Disaster and Climate Change

5 papers

Transferability of the ICHYMOD Model: A Case Study of Indrawati Catchment

Kshitiz Uchai[1*], Babu Ram Tiwari[1], Susen Shrestha[2]

[1]Department of Applied Sciences and Chemical Engineering, Pulchowk Campus, Institute of Engineering, Tribhuvan University
Lalitpur, Nepal
080msccd012.kshitiz@pcampus.edu.np, baburam.tiwari@pcampus.edu.np
[2]Consultant, Centre of Hydrology and Water Resources Research, Government of Nepal, Kathmandu, Nepal
susenshresth@gmail.com
[*]Corresponding author: 080msccd012.kshitiz@pcampus.edu.np; ORCID: https://orcid.org/0009-0002-8122-1173

Abstract

ICHYMOD is a semi-distributed hydrological model with an integrated snow and glacier module, TOPMELT, developed for flood forecasting of the snow-fed Adige river basin in Northern Italy. Although the model is semi-distributed, the enhanced temperature-index concept of TOPMELT resolves melt by elevation band and energy index, giving a fully distributed representation of snow and glacier melt that is crucial in alpine settings. It has been tested for the heavily glaciated Langtang basin; this work explores a slightly different mountain setting. The Indrawati catchment in central Nepal covers 1,146 km^2, spans 578 to 5,873 m a.s.l., is 1.43% glacierised, and feeds the Melamchi Water Supply Project. Given the sparse meteorological network, ERA5-Land reanalysis was used without bias correction and validated against the only daily discharge record, at Dolalghat. The catchment was divided into 27 elevation bands with 10 radiation classes each, and 30 parameters were calibrated by Monte Carlo Latin Hypercube Sampling of over 10,000 realisations. Simulated daily discharge for 2006 to 2024 gave R^2 = 0.811, NSE = 0.811, KGE = 0.866 and a bias of −1.4%. Snow-covered area compared with refined MODIS data gave contrasting results: good correlation during the winter and pre-monsoon snow season, and disagreement during the monsoon. Transfer of the Alpine-based ICHYMOD to the Himalayan Indrawati catchment is therefore promising, although the performance of uncorrected ERA5-Land remains an isolated case requiring testing in similar catchments. This study positions ICHYMOD as a better modelling option for mountainous catchments in Nepal compared with other modelling practices.

Keywords: ICHYMOD-TopMelt, ERA5-Land, model transferability, snowmelt modelling, data-scarce catchments, Melamchi Water Supply Project, Nepal Himalaya

Introduction

Himalayan river basins supply freshwater to large downstream populations through the combined action of monsoon precipitation, seasonal snow accumulation and glacier melt (Immerzeel et al., 2010). Monsoon rainfall delivers most of the annual water volume. Snowmelt and glacier melt sustain streamflow after the rainfall stops, and that seasonal buffering governs how much water remains available outside the monsoon. Rising temperatures and shifting precipitation are altering the balance between the two (Kayastha et al., 2020; Maskey et al., 2011), and national inventories record continued glacier retreat across Nepal (International Centre for Integrated Mountain Development [ICIMOD], 2014a, 2014b).

Simulating these changes requires a model that treats rainfall-runoff, snowmelt and ice melt as separate pathways. Much of the published hydrological work on Nepalese basins does not do this. Melt is either omitted or represented by a spatially uniform degree-day factor, which discards the two controls that organise melt in mountain terrain: the vertical temperature gradient, and the distribution of incoming solar radiation across slope and aspect. Models developed for Alpine catchments represent both explicitly, and several studies report that such models transfer to other glacierised mountain systems once recalibrated, because the governing processes recur across ranges even where the climatic forcing differs (Andrianaki et al., 2019; Argentin et al., 2025; Omani et al., 2017).

The Indrawati catchment makes the question an operational one. The basin supplies the Melamchi Water Supply Project, which diverts 170 MLD from the Melamchi River to the Kathmandu Valley. Second and third stage diversions of 170 MLD each are planned from the neighbouring Yangri and Larke rivers, which would bring total abstraction to 510 MLD (Bhattarai et al., 2015; Melamchi Water Supply Development Board [MWSDB], 2026). Published work on runoff generation in the basin remains limited. So does the meteorological basis for producing any. As across much of the Nepalese Himalaya, the monitoring network thins sharply with elevation, and the upper catchment that governs snow accumulation and melt timing carries no stations. A temperature field extrapolated upward from lower ground therefore rests on assumptions that cannot be verified where they matter.

This paper addresses two questions. Does ICHYMOD-TopMelt, an Alpine snow and glacier model, transfer to this catchment without structural modification, and is uncorrected ERA5-Land reanalysis sufficient to drive it? The forcing was kept minimal and uncorrected, and calibration used a single observed variable, so that the test measures the transferability of the model under freely available global input rather than the effect of a correction procedure layered on top of it. Answering both questions is a precondition for the more detailed work that follows from them, on how forcing preparation affects performance, how the snow component should be evaluated, and how runoff partitions between rainfall, snowmelt and ice melt. Those questions are treated separately.

Literature Review / Related Work

ICHYMOD-TopMelt is one of the Alpine models described above. It couples the topography-based snowpack module TOPMELT (Zaramella et al., 2019) with the semi-distributed conceptual rainfall-runoff model ICHYMOD (Norbiato et al., 2009). It was developed and tested in the Italian Alps, where it supports operational flood forecasting for the Province of Bolzano, and subsequent studies applied it to snowmelt simulation, snow-cover assimilation, seasonal predictability and the scale dependence of snow water equivalent error under reanalysis forcing (Dalla Torre et al., 2024; Di Marco et al., 2021; Shrestha et al., 2023; Stergiadi et al., 2020).

Devkota et al. (2026) reported the first application outside Italy, in the 352 km^2 Langtang catchment, where ERA5-Land forcing produced NSE values of 0.72 in calibration and 0.84 in validation. That study showed the model structure functions under a monsoon-influenced climate. Langtang is an unusual test case, though. Its outlet sits at 3,651 m a.s.l., higher than most of the ground in the catchment studied here, and it is 39% glacierised, so melt dominates the runoff signal. The model has not been tested in a larger, lower basin with a small glacier fraction, where snow and ice are secondary controls on flow. That configuration is the common

one across the Nepalese mid-hills, and it is the more consequential one for water resource assessment.

Reanalysis is the standard response to sparse high-elevation monitoring. ERA5-Land supplies spatially continuous hourly fields at roughly 9 km resolution (Muñoz-Sabater et al., 2021), and three studies establish its adequacy as hydrological forcing on both sides of the transferability question examined here. Dalla Torre et al. (2024) assessed it across Alpine catchments, Chen et al. (2021) evaluated reanalysis precipitation on the southern slope of the central Himalaya, and Devkota et al. (2026) drove a Himalayan model with it directly. Where a monitoring network cannot resolve the elevation gradient that controls melt, a spatially distributed reanalysis field is the more defensible input.

Materials and Methods

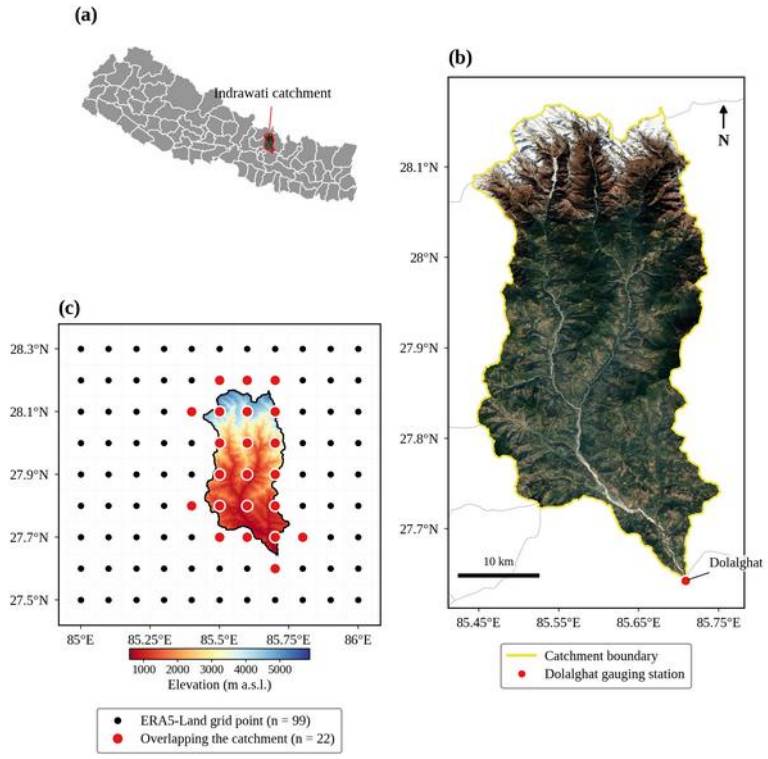
Study Area

The Indrawati basin lies in the central Himalayan region of Nepal, between 27.6° N and 28.16° N and between 85.44° E and 85.8° E. Delineated to the Dolalghat gauging station, which is the only discharge monitoring site in the basin and therefore the only point at which calibration is possible, the catchment covers 1,145.69 km^2 and spans elevations from 578 to 5,873 m a.s.l. High-altitude features including Baden Powell Peak, Ganja La and Ganchempo define its northern boundary. Glacier cover taken from the ICIMOD inventory amounts to 16.36 km^2, or 1.43% of catchment area (Figure 1).

A large elevation range combined with a small glacier fraction puts the Indrawati in a different hydrological regime from the heavily glacierised headwater basins where snow and ice models are usually applied in the Himalaya. Most of the catchment lies below the seasonal snowline for much of the year, and monsoon rainfall between June and September dominates runoff. Seasonal snow still accumulates over the upper bands through winter and releases through the pre-monsoon, adding to the spring rise in flow while rainfall is still low. The basin is therefore a mixed rainfall-snowmelt system in which the melt component is real but secondary, which is a demanding setting for a model built around melt-dominated Alpine catchments.

Figure 1

Study Area



Note. (a) Location of the Indrawati catchment within Nepal. (b) Catchment satellite imagery with the boundary and the Dolalghat gauging station at the outlet. (c) Catchment elevation with the 0.1° ERA5-Land grid; of the 99 domain points, 22 overlap the catchment.

Forcing and Reference Data

All meteorological forcing came from ERA5-Land (Muñoz-Sabater et al., 2021), obtained from the Copernicus Climate Data Store at hourly resolution and 0.1° (about 9 km) spatial resolution. Ninety-nine grid cells make up the extraction domain and 22 overlap the catchment (Figure 1c). Two-metre air temperature and total precipitation were extracted and aggregated to catchment means by fractional-area weighting, so each cell contributes in proportion to the share of the catchment it covers.

One treatment was applied to the precipitation series. ERA5-Land, like other reanalysis and climate model precipitation products, produces a long tail of very low-intensity wet values that inflates wet-day frequency relative to real precipitation. Hourly values below 0.1 mm were therefore set to zero before aggregation. This is a fixed-threshold frequency treatment, not a magnitude correction, and it needs no observational reference to define. Temperature was used as supplied. Neither variable was bias corrected against local measurements.

Observed daily discharge for calibration and evaluation came from the Department of Hydrology and Meteorology (DHM), Nepal, for the Dolalghat station (index 629.1). The record is incomplete over the simulation period. Both a simulated and an observed value exist on 4,292 days, and 2010 contains no usable observations. Glacier extent was prescribed from the ICIMOD inventory as a static fraction of each elevation band. Snow-cover reference data came from the ICIMOD improved 8-day, cloud-free Terra-Aqua MODIS product (MOD10A2/MYD10A2, Collection 6.1) for 2002 to 2022 (ICIMOD, 2023). This series was not used at any stage of calibration.

Model Description

ICHYMOD-TopMelt simulates snow water equivalent, glacier melt and discharge at an hourly time step, and it requires only temperature and precipitation as meteorological input. TOPMELT is an enhanced temperature-index scheme. In a classical degree-day model melt varies in space only through the temperature lapse rate. TOPMELT adds a clear-sky potential solar radiation term, so slope, aspect and topographic shading affect the spatial distribution of melt without requiring measured radiation or cloud data. The catchment is divided into elevation bands, which carry the variation of temperature with height, and each band is subdivided into equal-area radiation classes, with the *i*th class containing the sub-area corresponding to the *i*th percentile of incident radiation energy.

Daytime melt is the product of a combined melt factor, the cell radiation index, the daylight fraction, the complement of snow albedo, and the temperature excess above a base temperature. Snow albedo decays with accumulated positive temperature since the last snowfall, following Brock et al. (2000), which allows melt to accelerate through the ablation season without any change in air temperature. Separate factors govern night-time melt and rain-on-snow melt. Refreezing returns interstitial liquid water to the solid phase below the base temperature. Once a cell exhausts its seasonal snow, ice melt begins on the glacierised fraction of that cell, computed as for daytime melt but with a constant glacier albedo. Zaramella et al. (2019) give the full formulation.

Net water leaving the snowpack, together with rainfall on snow-free ground, passes to ICHYMOD. Its soil moisture routine uses the probability-distributed model of Moore (2007), in which point storage capacity follows a Pareto distribution, so the proportion of the basin generating direct runoff rises as the catchment wets up instead of staying fixed. Drainage recharges groundwater non-linearly, and a cubic-law storage model routes base discharge to the outlet with a recession constant that governs dry-season flow. A geomorphology-based distributed unit hydrograph routes direct runoff (Da Ros & Borga, 1997), and ice-melt runoff is divided between the soil store and a separate fast pathway. A Muskingum-Cunge scheme translates the combined contributions to the outlet. Evapotranspiration is computed from potential rates estimated by the Hargreaves method (Hargreaves & Samani, 1982) and reduced as the soil store depletes. Norbiato et al. (2009) give the full formulation.

Model Setup and Calibration

The basin was divided into 27 elevation bands of 200 m spanning 400 to 5,800 m a.s.l., with 10 radiation classes per band, giving 270 model cells. Glacier fraction was assigned per band from the ICIMOD inventory. The model was run at an hourly time step over 2006 to 2024, and simulated flows were aggregated to daily values on calendar dates for comparison against the observed record.

Thirty free parameters were calibrated by Monte Carlo sampling with Latin Hypercube Sampling (LHS). LHS stratifies each parameter axis independently and therefore covers a high-dimensional space more evenly than simple random sampling for a given number of model evaluations (McKay et al., 1979). Ten thousand parameter sets were generated within prescribed ranges. Two further parameters, the kinematic wave celerity and the routing reach length, were held fixed. Sampling ranges were informed by values reported for earlier applications of the same model (Devkota et al., 2026; Shrestha et al., 2023; Zaramella et al., 2019). Values were not

transferred directly, because the physiographic contrast between those catchments and the Indrawati makes direct transfer unwarranted.

Performance was evaluated with the coefficient of determination (R^2), Nash-Sutcliffe Efficiency (NSE; Nash & Sutcliffe, 1970), percent bias, and Kling-Gupta Efficiency (KGE; Gupta et al., 2009). KGE served as the objective function because it decomposes error into correlation, variability and bias components, and therefore does not reward one well-fitted component at the expense of the others. Table 1 gives calibrated values for the parameters that most influence melt and runoff generation.

Table 1

Selected ICHYMOD-TopMelt Parameters, Sampled Ranges and Calibrated Values

Parameter	Description	Range	Calibrated
CMF	Combined melt factor (mm °C^{-1} MJ^{-1} m^2 h^{-1})	0.006 to 0.025	0.0072
NMF	Night melt factor (mm °C^{-1} h^{-1})	0.04 to 0.30	0.136
ALBSNOW	Fresh-snow albedo (dimensionless)	0.60 to 0.95	0.700
ALBGLAC	Glacier albedo (dimensionless)	0.20 to 0.50	0.285
Tsnow	Snow-rain threshold temperature (°C)	0.5 to 3.0	2.108
Tmelt	Base temperature for melt (°C)	−0.5 to 0.5	−0.088
SCF	Snow correction factor (dimensionless)	1.1 to 2.5	2.086
PRECGRAD	Precipitation gradient with elevation (km^{-1})	0.00 to 0.50	0.480
B	Pareto exponent, soil storage distribution (dimensionless)	0.10 to 0.80	0.428
CMAX	Maximum point storage capacity (mm)	200 to 1000	950.95
KG	Groundwater recession constant (h)	20000 to 30000	29141
KGLAC	Residence time, glacial flow reservoirs (h)	0.5 to 8.0	0.739

Note. Monte Carlo calibration with Latin Hypercube Sampling, 10,000 realisations, KGE-optimal set. The full parameter set is provided as supplementary material.

Results

Discharge

The calibrated model reproduced observed daily discharge over 2006 to 2024 with R^2 = 0.811, NSE = 0.811, KGE = 0.866 and a mean bias of −1.02 m^3 s^{-1}. Against a mean observed discharge of about 73 m^3 s^{-1} this is a percent bias of −1.4%, so the simulated water balance is close to neutral across the record. Both NSE and percent bias fall in the “very good” class on the ratings of Moriasi et al. (2007). Annual KGE ranged from 0.402 in 2009 to 0.914 in 2018, with a mean of 0.745 over the 13 years for which a complete observed record exists (Table 2), and ten of those 13 years returned NSE above 0.62. One year performs poorly. The 2009 NSE of −1.853 sits against neighbouring values of 0.85 and 0.86, which points to a problem in the observed record rather than a failure of the simulation.

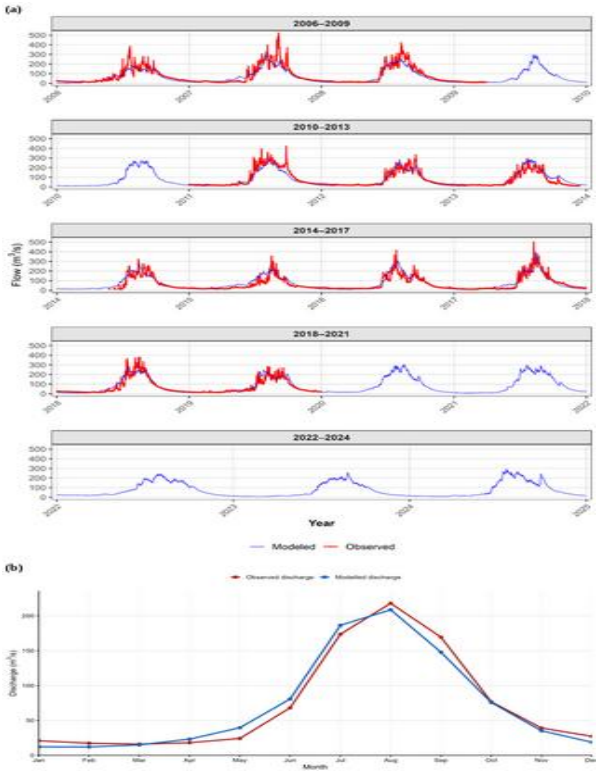
The residuals carry a seasonal structure that the aggregate statistics conceal. Simulated flow on the rising limb runs early and high, with April through July over-predicted. The largest errors occur in May, where the model gives about 40 m^3 s^{-1} against 25 m^3 s^{-1} observed, and in June, 81 against 68 m^3 s^{-1}. At the August peak the model turns slightly low, 209 against 217 m^3 s^{-1}, and the deficit widens through the recession to about 22 m^3 s^{-1} in September. Dry-season months are under-predicted by roughly 40% in January and February and 30% in December, although the

absolute quantities involved are small. March and October are reproduced almost exactly (Figure 2).

Taken together, these errors describe a modelled hydrograph displaced a few weeks earlier than the observed one, with too little water carried into the dry season. Melt begins too early in spring and draws down storage that would otherwise sustain the later monsoon, after which the recession empties the catchment faster than observed. The two errors have opposite sign and largely cancel over the year, which is why the annual water balance sits at −1.4% while individual monthly errors reach 60%. An aggregate metric such as KGE therefore cannot on its own confirm that the model partitions water correctly between its internal components.

Figure 2

Observed and Simulated Discharge at Dolalghat, 2006 to 2024



Note. (a) Observed and simulated daily discharge in four-year blocks; observed values are absent in 2010 and after 2019. (b) Monthly discharge climatology. Both panels use the same 4,292 paired daily values, for which R^2 = 0.811, NSE = 0.811, KGE = 0.866 and PBIAS = −1.4%.

Table 2

Year-by-Year Discharge Performance at Dolalghat

Year	R^2	NSE	KGE	Bias ($m^3 s^{-1}$)
2006	0.773	0.720	0.675	−14.44
2007	0.781	0.753	0.698	−8.54
2008	0.891	0.851	0.742	−13.28
2009	0.723	−1.853	0.402	−5.31
2011	0.908	0.857	0.730	−17.08
2012	0.878	0.874	0.906	−4.31

Year	R^2	NSE	KGE	Bias ($m^3 s^{-1}$)
2013	0.885	0.730	0.620	+20.11
2014	0.694	0.681	0.775	+8.17
2015	0.750	0.626	0.655	+17.01
2016	0.843	0.793	0.830	+4.87
2017	0.867	0.864	0.860	−3.97
2018	0.880	0.880	0.914	−0.05
2019	0.840	0.817	0.874	+5.56
Mean	0.824	0.584	0.745	n.a.

Note. 2010 is omitted because the observed record contains insufficient data to be scored. Coverage after 2019 is too sparse for complete-year statistics.

Snow-Covered Area

Simulated snow-covered area was compared against the MODIS reference. Because snow cover was withheld from calibration, this comparison tests independently whether the model divides precipitation correctly between rain and snow, rather than only reproducing the right total volume of flow. Agreement is moderate in winter (R^2 = 0.58, KGE = 0.40) and pre-monsoon (R^2 = 0.47, KGE = 0.48, PBIAS = −2.4%), the two seasons in which almost all of the catchment's snow accumulates and melts. The winter bias of +36% indicates that the model over-estimates cold-season snow extent relative to the satellite record, while the near-neutral pre-monsoon balance indicates that it captures the timing and magnitude of the spring melt-out. Skill falls away in monsoon (R^2 = 0.08, KGE = −0.55) and post-monsoon (R^2 = 0.32, KGE = −0.67). Mean MODIS fractional snow cover holds at 0.14 through the monsoon while mean modelled cover falls to 0.03, a bias of −80%. The pattern repeats every year: monsoon KGE is negative in all 17 years, with PBIAS between −69% and −87% (Table 3).

The cold-season agreement is not merely an average. Resolving the seasonal skill into individual years (Figure 4) shows winter KGE positive in 15 of 17 years and pre-monsoon KGE positive in 16 of 17, with pre-monsoon exceeding 0.5 in 9 years. The warm seasons show no such recovery: monsoon KGE is negative in every year, and post-monsoon KGE is negative in every year except 2013, where it is close to zero. The correspondence with discharge is clearest among the best-simulated years: of the four years with the highest discharge KGE (2012, 2017, 2018 and 2019, all above 0.86), three also carry strong skill in both cold seasons. In 2012, 2017 and 2019 winter KGE is 0.71, 0.51 and 0.67, pre-monsoon KGE is 0.59, 0.75 and 0.78, and the winter bias is small (+17%, +8% and +6%). That the snow component and the discharge component agree independently in the same years is the clearest single indication that the calibrated model reproduces the basin's hydrology for the right physical reasons, rather than compensating a snow error against a rainfall error to fit the gauge.

The fourth year is the informative exception. 2018 pairs the highest discharge KGE of the record (0.914) with a poor winter SCA KGE (−0.148) and a winter bias of +93%, the largest in the series. The discharge is therefore reproduced that year in spite of a substantial cold-season snow error, which is precisely the compensating behaviour the independent snow comparison exists to expose. Its presence alongside the three clean years shows that the agreement in 2012, 2017 and 2019 is a genuine result rather than an artefact of the comparison, and that snow cover carries information the discharge record alone cannot. Across the 13 years for which both are available the year-to-year association is positive but loose (correlation of winter snow-cover and discharge

KGE r = 0.4), so the pattern is best read as a tendency for the strongest discharge years to be strong snow years, not as a predictive relationship.

Table 3

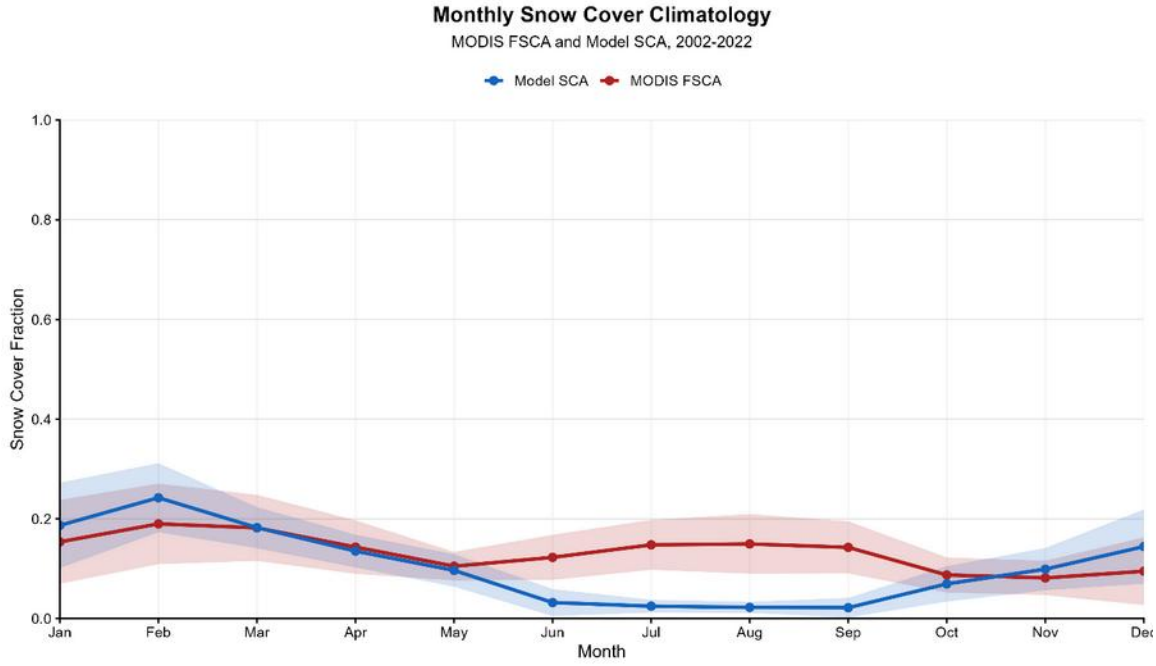
Seasonal Comparison of Modelled Snow-Covered Area Against MODIS Fractional Snow-Covered Area, 2006 to 2022

Season	MODIS FSCA	Model SCA	R^2	KGE	PBIAS (%)
Winter	0.146	0.191	0.583	0.404	+36.3
Pre-monsoon	0.144	0.139	0.471	0.475	−2.4
Monsoon	0.140	0.026	0.077	−0.545	−80.5
Post-monsoon	0.105	0.062	0.318	−0.672	−41.6

Note. Values are averaged across 2006 to 2022 (17 years per season; ICIMOD 8-day MOD10A2/MYD10A2 product). Seasons are winter (DJF), pre-monsoon (MAM), monsoon (JJAS) and post-monsoon (ON). Snow cover was not used in calibration.

Figure 3

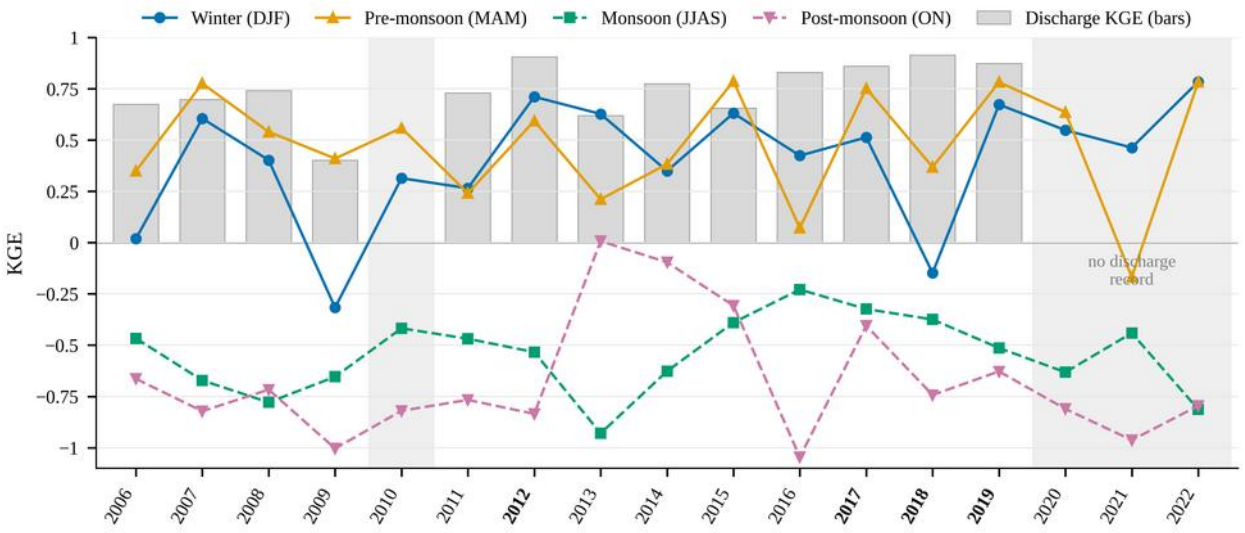
Monthly Climatology of MODIS and Modelled Snow-Covered Area, 2006 to 2022



Note. Shaded bands show ±1 standard deviation across years.

Figure 4

Year-by-Year Seasonal Snow-Cover Skill and Annual Discharge Skill, 2006 to 2022



Note. Lines show KGE of modelled snow-covered area against MODIS fractional snow cover for winter (DJF), pre-monsoon (MAM), monsoon (JJAS) and post-monsoon (ON). Grey bars show annual discharge KGE at Dolalghat for the discharge-best forcing configuration. Shaded columns mark years without a scorable discharge record (2010 and 2020 to 2022). Bold year labels mark the four best-simulated discharge years (2012, 2017, 2018 and 2019). Three of them also carry strong cold-season snow-cover skill; 2018 pairs the highest discharge skill with a poor winter snow-cover fit (bias +93%).

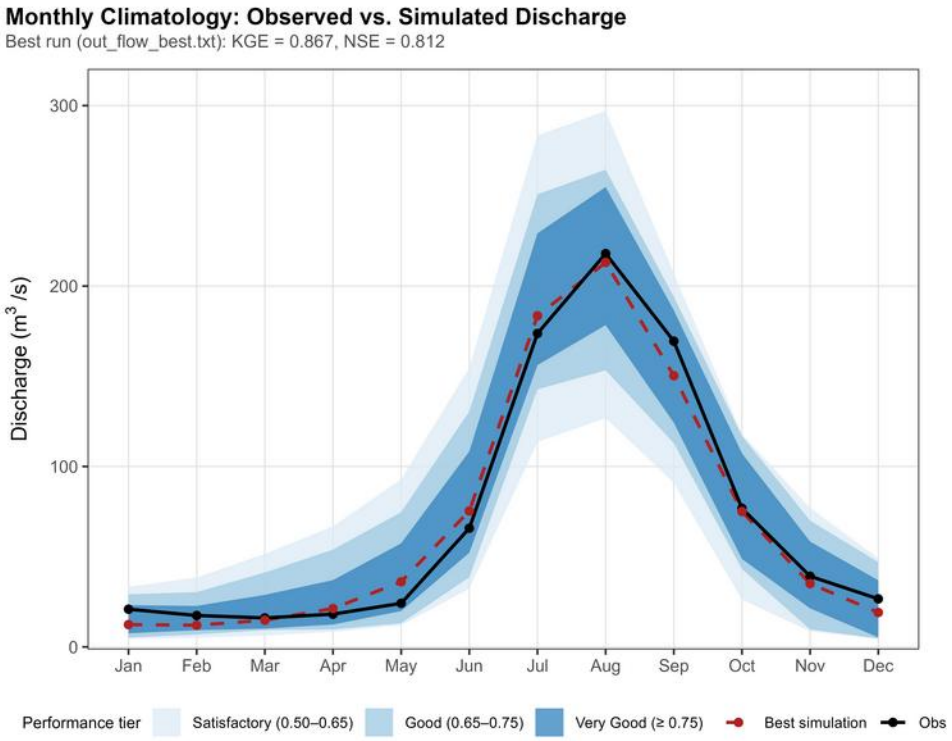
Two explanations of the warm-season disagreement are consistent with the available evidence, and this comparison cannot distinguish them. The catchment is 1.43% glacierised and most of its area lies well below the monsoon snowline, so near-zero warm-season snow cover is physically plausible, which would imply a positive bias in the satellite reference. Reflectance-based retrievals are known to perform poorly under sustained cloud, and cloud–snow confusion is a principal source of commission error in MODIS snow products (Hall & Riggs, 2007; Stillinger et al., 2019). Eight-day MODIS composites still retain substantial cloud during the monsoon (Muhammad & Thapa, 2020). In the neighbouring Langtang catchment, a MODIS product filtered in time and space remained contaminated by cloud misclassified as snow during the monsoon; time-lapse cameras placed the monsoon snowline well above the MODIS estimate, and monsoon scenes were excluded from the evaluation (Saloranta et al., 2019). Shrestha et al. (2012) likewise discarded MODIS scenes after early June in the Dudh Koshi. The 500 m pixels also tend to overestimate snow extent in steep, heterogeneous terrain (Ghimire et al., 2026; Tang et al., 2013). Alternatively, the model may melt the high-elevation snowpack too readily under monsoon temperatures. Simulated snow cover in sparsely gauged Himalayan catchments is sensitive to the temperature lapse rate, the snow–rain threshold temperature and the precipitation gradient (Immerzeel et al., 2014; Zhang et al., 2015), none of which is constrained here by high-elevation observations. That the pattern repeats in every year of the record indicates a systematic cause rather than year-specific model error, but it does not identify which cause.

The two annual cycles side by side (Figure 2b and Figure 3) summarise where the transferred model tracks the observations and where it does not. The mean monthly hydrograph is followed closely through the whole year, including the low-flow winter months, while the mean snow-

cover cycle is followed through the accumulation and melt season, from the winter maximum to the pre-monsoon decline, and departs from the satellite record only in the monsoon and early post-monsoon, when modelled cover falls to near zero while the MODIS series shows a secondary mid-summer rise, a feature consistent with residual cloud contamination (Saloranta et al., 2019). Figure 5 extends the discharge comparison across the full calibration ensemble: shaded bands show the min–max envelope of the 10,000-member Monte Carlo ensemble, which represents parameter equifinality (Beven & Binley, 1992; Beven & Freer, 2001), grouped into three tiers by joint NSE–KGE performance classification (Satisfactory, Good, Very Good; Moriasi et al., 2007).

Figure 5

Monthly Climatology of Observed and Simulated Discharge, 2006 to 2024



Note. Shaded bands show the min–max envelope of the full Monte Carlo calibration ensemble split into three performance tiers (Satisfactory, Good, Very Good) by joint NSE–KGE classification; the dashed line is the KGE-optimal (best) simulation.

Discussion

Model Transfer

A KGE of 0.866 and a percent bias of −1.4% over an 18-year record are comparable to what ICHYMOD-TopMelt achieves in the Alpine basins for which it was built, and higher than the values Devkota et al. (2026) obtained in Langtang. The two are not directly comparable. Langtang is smaller, higher and far more heavily glacierised, so melt carries a much larger share of its runoff signal and is correspondingly harder to reproduce. The transfer is nonetheless consistent with what the model represents. Elevation-dependent temperature, radiation-weighted

melt distribution, albedo ageing, snowpack liquid water retention and saturation-excess runoff generation are the same physical processes in the Himalaya as in the Alps, operating under different boundary conditions. The climatic forcing differs, as does the weight of melt against direct rainfall and the elevation distribution of the catchment, and parameter values absorb all three without requiring changes to model structure. The calibrated set stays physically interpretable, with melt factors, albedo coefficients and threshold temperatures inside the ranges reported for the model elsewhere.

The independent snow-cover comparison supports this within the season it can. Through winter and pre-monsoon, when almost all of the catchment's snow accumulates and melts, the model follows the observed seasonal cycle and the pre-monsoon water balance is close to neutral. Snow cover was withheld from calibration, so this indicates that good discharge statistics do not arise from a compensating misallocation between rain and snow. The year-by-year correspondence strengthens the point: three of the four best-simulated discharge years are also years in which cold-season snow cover is reproduced well, so the two independent lines of evidence agree where it matters most, while the fourth (2018) shows the comparison is still able to flag a compensating snow error. The monsoon disagreement is unresolved rather than diagnostic. Describing it as model failure would overstate what the comparison shows, given how unreliable optical retrievals are under persistent cloud, and describing it as a satellite artefact would overstate the case in the absence of an independent snow observation to arbitrate.

Adequacy of Uncorrected Reanalysis

This performance was obtained with no local correction of the forcing. ERA5-Land supplied a spatially continuous field across the full elevation range of the catchment, including high ground where no measurements exist, and the only treatment applied was a fixed threshold removing spurious low-intensity precipitation, which needs no observational reference and is reproducible in any catchment. For a basin whose upper zone carries no stations, this is the practically useful finding. Process-based melt modelling is available in the Indrawati now, without waiting for a monitoring network to be built.

The reported values are therefore a lower bound rather than the best the configuration can achieve. Bias correction of the ERA5-Land temperature and precipitation series should improve on them. How much improvement is available, and which correction method delivers it, is a substantial question in itself. The seasonal residual structure reported for discharge in the Results, with early melt on the rising limb and insufficient carry-over into the dry season, indicates where that improvement would be most useful.

Further Work

Three lines of work follow from these results. The first is a systematic evaluation of forcing preparation, comparing bias-corrected reanalysis against the uncorrected series used here and establishing whether the choice matters more for temperature or for precipitation. The second is resolution of the monsoon snow-cover disagreement, which needs a product with better cloud handling and finer resolution than the 8-day composite available here, ideally supported by in-situ snow observation at elevation. The third is extraction of the runoff partitioning between rainfall, snowmelt and ice melt that the model already computes internally for each elevation and radiation band. That last is a modest extension of existing output and a prerequisite for assessing how the melt contribution to dry-season flow at the Melamchi diversion sites may change.

Limitations

The observational basis is thin, which constrains the strength of these conclusions rather than their direction. No meteorological measurements exist in the upper catchment, so the forcing could not be checked against local observations at the elevations where snow accumulates, and the model was calibrated against one variable at one point. The discharge record contains gaps, including a complete absence of usable data for 2010.

Several calibrated parameters settled at or near the edge of their sampled ranges. For these the reported value is the best available within the bounds searched, not an unconstrained optimum. Ten thousand samples is also modest for a space of 30 free dimensions, so the calibrated set should be read as one good solution rather than as the solution, and no formal equifinality or uncertainty analysis was performed.

ICHYMOD-TopMelt is a conceptual model. It does not represent snow redistribution by wind, sublimation, avalanching or the insulating effect of debris-covered ice, and glacier extent is prescribed as static rather than evolving through the simulation. These omissions matter less in a catchment that is 1.43% glacierised than they would elsewhere, but they still bound how far the simulated cryospheric processes should be interpreted. Resolution differences between the ERA5-Land grid, the model elevation bands and the MODIS product add further uncertainty (Avesani et al., 2025).

Conclusion

ICHYMOD-TopMelt, a snow and glacier hydrological model developed and used operationally in the Italian Alps, was applied to the Indrawati catchment in the Nepalese Lesser Himalaya. The model was driven entirely by uncorrected ERA5-Land reanalysis and calibrated by Monte Carlo Latin Hypercube Sampling against observed discharge at Dolalghat. It reproduced observed daily discharge over 2006 to 2024 with $R^2 = 0.811$, NSE = 0.811, KGE = 0.866 and a percent bias of −1.4%, placing both NSE and percent bias in the “very good” class, and returned a mean annual KGE of 0.745 across 13 complete years. An independent comparison against MODIS snow cover gave moderate agreement in winter and pre-monsoon, when almost all of the catchment's snow occurs, and unresolved disagreement through the monsoon; the best discharge years were generally also years of strong cold-season snow-cover skill.

Two findings follow. The model transfers from its Alpine origin to a large, monsoon-dominated catchment with a small glacier fraction, without structural modification, and its calibrated parameter set stays physically interpretable. This extends the evidence for transferability beyond the single previous Himalayan application, which used a small and heavily glacierised headwater basin. Uncorrected global reanalysis is also sufficient forcing for this purpose, which means process-based melt modelling can proceed in the basin now rather than waiting on a high-elevation monitoring network.

Neither finding closes the enquiry. The forcing was uncorrected and calibration rested on a single variable, so the performance reported here is a lower bound, and the seasonal residual structure indicates where improvement should be sought. What the results establish is that the modelling framework performs well enough in this catchment to support the more detailed evaluation of forcing preparation, snow-process representation and runoff partitioning that the basin's role in the Melamchi Water Supply Project makes worth undertaking.

Acknowledgments

The authors thank the Department of Hydrology and Meteorology, Nepal, for providing the Dolalghat discharge record, and ICIMOD for the glacier inventory and MODIS snow-cover products. During the preparation of this work the authors used Claude (Anthropic) to debug analysis code for data processing and draft codes for figure generation in R and Python, and for language editing of the manuscript. The authors reviewed and edited the content as needed and take full responsibility for the content of the publication.

Funding

The authors received no financial support for the research, authorship, or publication of this paper.

Conflict of Interest

The authors declare no conflict of interest.

Author Contributions

Kshitiz Uchai: conceptualization, methodology, software, formal analysis, investigation, visualization, writing (original draft). Babu Ram Tiwari: supervision, writing (review and editing). Susen Shrestha: conceptualization, methodology, supervision, writing (review and editing).

Data Availability

ERA5-Land reanalysis data are freely available from the Copernicus Climate Data Store. The ICIMOD glacier inventories and MODIS snow-cover product are available from the ICIMOD Regional Database System. Observed discharge for the Dolalghat station was obtained from the Department of Hydrology and Meteorology, Nepal, and is available from that department on request. Model configuration files and simulation outputs are available from the corresponding author on reasonable request.

References

Andrianaki, M., Shrestha, J., Kobierska, F., Nikolaidis, N. P., & Bernasconi, S. M. (2019). Assessment of SWAT spatial and temporal transferability for a high-altitude glacierized catchment. *Hydrology and Earth System Sciences, 23*(8), 3219–3232. https://doi.org/10.5194/hess-23-3219-2019

Argentin, A.-L., Horton, P., Schaefli, B., Shokory, J., Pitscheider, F., Repnik, L., Gianini, M., Bizzi, S., Lane, S. N., & Comiti, F. (2025). Scale dependency in modeling nivo-glacial hydrological systems: The case of the Arolla basin, Switzerland. *Hydrology and Earth System Sciences, 29*(6), 1725–1748. https://doi.org/10.5194/hess-29-1725-2025

Avesani, D., Nan, Y., & Tian, F. (2025). Reducing hydrological uncertainty in large mountainous basins: The role of isotope, snow cover, and glacier dynamics in capturing streamflow seasonality. *Hydrology and Earth System Sciences, 29*(20), 5755–5775. https://doi.org/10.5194/hess-29-5755-2025

Beven, K., & Binley, A. (1992). The future of distributed models: Model calibration and uncertainty prediction. *Hydrological Processes, 6*(3), 279–298. https://doi.org/10.1002/hyp.3360060305

Beven, K., & Freer, J. (2001). Equifinality, data assimilation, and uncertainty estimation in mechanistic modelling of complex environmental systems using the GLUE methodology. *Journal of Hydrology, 249*(1–4), 11–29. https://doi.org/10.1016/S0022-1694(01)00421-8

Bhattarai, G., Lees, D., & Niaz, A. (2015). *The Melamchi Water Supply Project* [Conference paper].

Brock, B. W., Willis, I. C., & Sharp, M. J. (2000). Measurement and parameterization of albedo variations at Haut Glacier d'Arolla, Switzerland. *Journal of Glaciology, 46*(155), 675–688. https://doi.org/10.3189/172756500781832675

Chen, Y., Sharma, S., Zhou, X., Yang, K., Li, X., Niu, X., Hu, X., & Khadka, N. (2021). Spatial performance of multiple reanalysis precipitation datasets on the southern slope of central Himalaya. *Atmospheric Research, 250*, Article 105365. https://doi.org/10.1016/j.atmosres.2020.105365

Da Ros, D., & Borga, M. (1997). Use of digital elevation model data for the derivation of the geomorphological instantaneous unit hydrograph. *Hydrological Processes, 11*(1), 13–33. https://doi.org/10.1002/(SICI)1099-1085(199701)11:1<13::AID-HYP400>3.0.CO;2-M

Dalla Torre, D., Di Marco, N., Menapace, A., Avesani, D., Righetti, M., & Majone, B. (2024). Suitability of ERA5-Land reanalysis dataset for hydrological modelling in the Alpine region. *Journal of Hydrology: Regional Studies, 52*, Article 101718. https://doi.org/10.1016/j.ejrh.2024.101718

Devkota, A., Bhattarai, P. K., Pandey, V. P., Pichuka, S., Pradhan, A. M. S., & Shrestha, S. (2026). Hydrological performance of ERA5-Land in the data-scarce Himalayan region of the Langtang catchment. *Theoretical and Applied Climatology, 157*(1), Article 14. https://doi.org/10.1007/s00704-025-05933-x

Di Marco, N., Avesani, D., Righetti, M., Zaramella, M., Majone, B., & Borga, M. (2021). Reducing hydrological modelling uncertainty by using MODIS snow cover data and a topography-based distribution function snowmelt model. *Journal of Hydrology, 599*, Article 126020. https://doi.org/10.1016/j.jhydrol.2021.126020

Ghimire, M., Shrestha, D., Chauhan, R., Thapa, A., Sharma, T. P. P., Sharma, K. P., Gurung, S. B., Devkota, S., Bhandari, P., Koirala, S., Wu, Y., Timalsina, N., & Kutu, J. (2026). Dynamics of snow and glacier cover in the Upper Karnali Basin, Nepal: An analysis of its relationship with climatic and topographic parameters. *The Cryosphere, 20*(1), 551–572. https://doi.org/10.5194/tc-20-551-2026

Gupta, H. V., Kling, H., Yilmaz, K. K., & Martinez, G. F. (2009). Decomposition of the mean squared error and NSE performance criteria: Implications for improving hydrological modelling. *Journal of Hydrology, 377*(1–2), 80–91. https://doi.org/10.1016/j.jhydrol.2009.08.003

Hall, D. K., & Riggs, G. A. (2007). Accuracy assessment of the MODIS snow products. *Hydrological Processes, 21*(12), 1534–1547. https://doi.org/10.1002/hyp.6715

Hargreaves, G. H., & Samani, Z. A. (1982). Estimating potential evapotranspiration. *Journal of the Irrigation and Drainage Division, 108*(3), 225–230. https://doi.org/10.1061/JRCEA4.0001390

Immerzeel, W. W., Petersen, L., Ragettli, S., & Pellicciotti, F. (2014). The importance of observed gradients of air temperature and precipitation for modeling runoff from a glacierized watershed in the Nepalese Himalayas. *Water Resources Research, 50*(3), 2212–2226. https://doi.org/10.1002/2013WR014506

Immerzeel, W. W., van Beek, L. P. H., & Bierkens, M. F. P. (2010). Climate change will affect the Asian water towers. *Science, 328*(5984), 1382–1385. https://doi.org/10.1126/science.1183188

International Centre for Integrated Mountain Development. (2014a). *Glaciers of Nepal 1980* [Data set]. https://doi.org/10.26066/rds.9349

International Centre for Integrated Mountain Development. (2014b). *Glaciers of Nepal 2010* [Data set]. https://doi.org/10.26066/RDS.9352

International Centre for Integrated Mountain Development. (2023). *Improved 8-day version 6.1 Terra-Aqua MODIS cloud-free snow cover and Randolph Glacier Inventory 6.0 product for high-mountain Asia between 2002 and 2022* [Data set].

Kayastha, R. B., Steiner, N., Kayastha, R., Mishra, S. K., & McDonald, K. (2020). Comparative study of hydrology and icemelt in three Nepal river basins using the Glacio-Hydrological Degree-Day Model (GDM) and observations from the Advanced Scatterometer (ASCAT). *Frontiers in Earth Science, 7*, Article 354. https://doi.org/10.3389/feart.2019.00354

Maskey, S., Uhlenbrook, S., & Ojha, S. (2011). An analysis of snow cover changes in the Himalayan region using MODIS snow products and in-situ temperature data. *Climatic Change, 108*(1–2), 391–400. https://doi.org/10.1007/s10584-011-0181-y

McKay, M. D., Beckman, R. J., & Conover, W. J. (1979). A comparison of three methods for selecting values of input variables in the analysis of output from a computer code. *Technometrics, 21*(2), 239–245. https://doi.org/10.1080/00401706.1979.10489755

Melamchi Water Supply Development Board. (2026). *Project description*. Retrieved August 2026, from http://www.melamchiwater.gov.np

Moore, R. J. (2007). The PDM rainfall-runoff model. *Hydrology and Earth System Sciences, 11*(1), 483–499. https://doi.org/10.5194/hess-11-483-2007

Moriasi, D. N., Arnold, J. G., Van Liew, M. W., Bingner, R. L., Harmel, R. D., & Veith, T. L. (2007). Model evaluation guidelines for systematic quantification of accuracy in watershed simulations. *Transactions of the ASABE, 50*(3), 885–900. https://doi.org/10.13031/2013.23153

Muhammad, S., & Thapa, A. (2020). An improved Terra–Aqua MODIS snow cover and Randolph Glacier Inventory 6.0 combined product (MOYDGL06*) for high-mountain Asia between 2002 and 2018. *Earth System Science Data, 12*(1), 345–356. https://doi.org/10.5194/essd-12-345-2020

Muñoz-Sabater, J., Dutra, E., Agustí-Panareda, A., Albergel, C., Arduini, G., Balsamo, G., Boussetta, S., Choulga, M., Harrigan, S., Hersbach, H., Martens, B., Miralles, D. G., Piles, M., Rodríguez-Fernández, N. J., Zsoter, E., Buontempo, C., & Thépaut, J.-N. (2021). ERA5-Land: A state-of-the-art global reanalysis dataset for land applications. *Earth System Science Data, 13*(9), 4349–4383. https://doi.org/10.5194/essd-13-4349-2021

Nash, J. E., & Sutcliffe, J. V. (1970). River flow forecasting through conceptual models part I: A discussion of principles. *Journal of Hydrology, 10*(3), 282–290. https://doi.org/10.1016/0022-1694(70)90255-6

Norbiato, D., Borga, M., Merz, R., Blöschl, G., & Carton, A. (2009). Controls on event runoff coefficients in the eastern Italian Alps. *Journal of Hydrology, 375*(3–4), 312–325. https://doi.org/10.1016/j.jhydrol.2009.06.044

Omani, N., Srinivasan, R., Karthikeyan, R., & Smith, P. (2017). Hydrological modeling of highly glacierized basins (Andes, Alps, and Central Asia). *Water, 9*(2), Article 111. https://doi.org/10.3390/w9020111

Saloranta, T., Thapa, A., Kirkham, J. D., Koch, I., Melvold, K., Stigter, E., Litt, M., & Møen, K. (2019). A model setup for mapping snow conditions in high-mountain Himalaya. *Frontiers in Earth Science, 7,* Article 129. https://doi.org/10.3389/feart.2019.00129

Shrestha, M., Wang, L., Koike, T., Xue, Y., & Hirabayashi, Y. (2012). Modeling the spatial distribution of snow cover in the Dudhkoshi region of the Nepal Himalayas. *Journal of Hydrometeorology, 13*(1), 204–222. https://doi.org/10.1175/JHM-D-10-05027.1

Shrestha, S., Zaramella, M., Callegari, M., Greifeneder, F., & Borga, M. (2023). Scale dependence of errors in snow water equivalent simulations using ERA5 reanalysis over alpine basins. *Climate, 11*(7), Article 154. https://doi.org/10.3390/cli11070154

Stergiadi, M., Di Marco, N., Avesani, D., Righetti, M., & Borga, M. (2020). Impact of geology on seasonal hydrological predictability in alpine regions by a sensitivity analysis framework. *Water, 12*(8), Article 2255. https://doi.org/10.3390/w12082255

Stillinger, T., Roberts, D. A., Collar, N. M., & Dozier, J. (2019). Cloud masking for Landsat 8 and MODIS Terra over snow-covered terrain: Error analysis and spectral similarity between snow and cloud. *Water Resources Research, 55*(7), 6169–6184. https://doi.org/10.1029/2019WR024932

Tang, B.-H., Shrestha, B., Li, Z.-L., Liu, G., Ouyang, H., Gurung, D. R., Giriraj, A., & Aung, K. S. (2013). Determination of snow cover from MODIS data for the Tibetan Plateau region. *International Journal of Applied Earth Observation and Geoinformation, 21*, 356–365. https://doi.org/10.1016/j.jag.2012.07.014

Zaramella, M., Borga, M., Zoccatelli, D., & Carturan, L. (2019). TOPMELT 1.0: A topography-based distribution function approach to snowmelt simulation for hydrological modelling at basin scale. *Geoscientific Model Development, 12*(12), 5251–5265. https://doi.org/10.5194/gmd-12-5251-2019

Zhang, F., Zhang, H., Hagen, S. C., Ye, M., Wang, D., Gui, D., Zeng, C., Tian, L., & Liu, J. (2015). Snow cover and runoff modelling in a high mountain catchment with scarce data: Effects of temperature and precipitation parameters. *Hydrological Processes, 29*(1), 52–65. https://doi.org/10.1002/hyp.10125

Assessing the Relationship Between NDVI and LST in Kathmandu Valley: A Geospatial Analysis of 2025

Kiran Dhungana[1]

[1]Department of Applied Sciences and Chemical Engineering, Pulchowk Campus, Institute of Engineering, Tribhuvan University
Lalitpur, Nepal
081msccd005.kiran@pcampus.edu.np/ ORCID ID: 0009-0009-6237-7157

Abstract

Changes in thermal environment in urban areas are brought about by urbanization and land-cover change. however, vegetation can play an important role in reducing surface heating through shading and evapotranspiration. This study examines the relationship between normalized difference vegetation index (NDVI) and land surface temperature (LST) in Kathmandu Valley, Nepal for 2025 and investigate the seasonal variations. The NDVI was obtained through analysis of Sentinel-2 satellite imagery while LST was derived from Landsat 8/9 Collection 2 Level-2 Thermal data through Google Earth Engine. To examine the relationship between NDVI and LST, 500 random samples were analyzed using the Pearson's correlation coefficient (r) and coefficient of determination (R^2). Negative correlation existed between NDVI and LST ($r = -0.755$, $R^2 = 0.570$). Pre-monsoon season had the highest negative correlation ($r = -0.776$, $R^2 = 0.602$) between NDVI and LST, followed by post-monsoon season ($r = -0.714$, $R^2 = 0.509$). Negative correlation in winter was $r = (-0.609$, $R^2 = 0.371$) while monsoon season showed almost no correlation ($r = +0.039$, $R^2 = 0.002$).

Keywords: Land Surface Temperature (LST), Normalized Difference Vegetation Index (NDVI), Urban Vegetation, Seasonal Variability, Kathmandu Valley

Introduction

Urbanization and land cover change can modify the thermal regime of the city and induce the urban heat island (UHI) phenomenon (Oke, 1982; Voogt & Oke, 2003). The development of impervious surfaces and changes in the coverage of vegetation have impacts on the surface energy budget and determine the distribution of LST. Satellite remote sensing has been widely used to investigate urban thermal patterns and the urban heat island phenomenon at different spatial scales (Voogt & Oke, 2003; Weng, 2009).

Urban vegetation can play a role in reducing the heating of the surface through shading and evapotranspiration; therefore, it is a crucial element that should be taken into account during the planning of urban climate responsive city (Gill et al., 2007; Bowler et al., 2010). NDVI is a popular way of evaluating the greening of the land surface based on satellite imagery (Rouse et al., 1974). Several studies have already employed NDVI and LST in combination to examine the relations of vegetation, land cover characteristics, and urban thermal regimes (Sarif et al., 2020; Bhandari & Zhang, 2022).

Vegetation dynamics and urban surface temperature have been studied previously in Kathmandu Valley. For instance, Sharma et al. (2018) carried out a study on the seasonality of NDVI and vegetation changes in Kathmandu Valley from 2000 to 2015. Sarif et al. (2020) analyzed land use/land cover changes and their associations with surface urban heat islands from 1988 to 2018. On the other hand, Aryal et al. (2021) performed the analysis of LST using Landsat in

Kathmandu Valley from 2013 to 2019. These studies provide a regional framework in analyzing vegetation dynamics and urban thermal conditions. Nonetheless, the differences in their timeframes, research goals, and methodology may warrant more research on the seasonality of NDVI and LST.

The objective of the research is to determine the correlation of NDVI with LST in Kathmandu Valley for 2025 through the use of satellite images from Sentinel-2 and Landsat 8/9 via Google Earth Engine. The study focuses on the general correlation of NDVI and LST and seasonal changes from January to February (winter season), March to May (pre-monsoon season), June to September (monsoon season), and October to December (post-monsoon season).

Literature Review

Remote sensing using satellites is extensively employed in studying the urban thermal environment and land use-LST association. Voogt and Oke (2003) described the application of remote sensing techniques in thermal research within the urban climate field, while Weng (2009) provided an overview of its techniques and applications in urban heat island studies. NDVI is widely used as an indicator of vegetation greenness, and its association with LST helps establish a pattern of surface warming. The effect of vegetation on surface temperature can be due to shading and evapotranspiration processes, among other factors.

A number of researches have been conducted regarding the vegetation dynamics, land cover changes, and LST in Kathmandu valley. The research done by Sharma et al. (2018) focuses on the seasonal and long-term trends of vegetation indices from 2000 to 2015 which give information about the dynamics of vegetation greenness. In addition to that, Sarif et al. (2020) conduct research on land use and land cover changes, and LST between 1988 and 2018 based on satellite imagery. The results have revealed the connection between the urban growth, land cover changes, and surface urban heat islands pattern. Aryal et al. (2021) have researched LST based on satellite imagery in Kathmandu valley. These researches provide the background of the thermal environment in Kathmandu Valley. Nevertheless, the focus of these researches on vegetation trends, land cover changes over the long period of time, and LST patterns reveal the importance of studying the connection between vegetation greenness and surface temperature over specific seasons.

While previous researches have investigated vegetation dynamics and surface temperatures of Kathmandu Valley, the current study will provide an additional perspective by assessing the connection between NDVI and LST for four seasons using satellite imagery from 2025. It is vital to conduct the research with the help of season-based approach as the link between vegetation and surface temperatures can differ at different times of the year. In this respect, the current paper will use Sentinel-2 NDVI and Landsat 8/9 LST datasets within Google Earth Engine to evaluate the relationship between the mentioned factors.

Materials and Methods

Study Design and Sources of Data

This study has used a quantitative approach with satellite data to examine the spatial association of NDVI with LST in a rectangular study area of Kathmandu Valley, Nepal (85.25°–85.45° E, 27.60°–27.80° N). NDVI was derived using Sentinel-2 Surface Reflectance Harmonized imagery and LST was estimated using Landsat Collection 2 Level-2 imagery. The analysis was carried

out for four seasons of 2025 i.e. winter (January-February), pre-monsoon (March-May), monsoon (June-September) and post-monsoon (October-December).

Satellite Data and Image Processing

Sentinel-2 Surface Reflectance NDVI was derived from harmonized imagery, while LST was estimated using Landsat 8 and Landsat 9 Collection 2 Level-2 imagery. Image collections were filtered by the study area boundary, acquisition dates, and scene-level cloud cover thresholds. Sentinel-2 scenes with cloud cover below 20% were selected, while Landsat 8 and Landsat 9 scenes with reported cloud cover below 70% were selected and merged into a single collection. The same approach was applied to all seasons; however, the availability of suitable satellite imagery varied seasonally, particularly during the monsoon period.

Derivation of NDVI and Land Surface Temperature (LST)

The Normalized Difference Vegetation Index (NDVI) was derived from Sentinel-2 Surface Reflectance Harmonized imagery using the near-infrared (Band 8) and red (Band 4) spectral bands. NDVI was calculated using Equation (1):

Higher positive NDVI values generally indicate greater vegetation greenness, whereas values closer to zero or negative values may indicate sparse vegetation, bare surfaces, water, or other non-vegetated features (Rouse et al., 1974).

Land surface temperature (LST) was derived from Landsat 8 and Landsat 9 Collection 2 Level-2 imagery using the ST_B10 surface-temperature band. The scaled band values were converted to Kelvin using the scale factor and offset specified for Landsat Collection 2 surface-temperature products, as shown in Equation (2):

The temperature was subsequently converted from Kelvin to degrees Celsius using Equation (3):

The resulting NDVI and LST layers were combined to examine their spatial relationship. A random sample of 500 points was generated within the study area at a nominal spatial scale of 30 m, using a fixed random seed of 42. The satellite-image processing and calculations were performed in Google Earth Engine (Gorelick et al., 2017).

Spatial Sampling and Statistical Analysis

A fixed set of 500 random spatial sample points was generated within the study area using a fixed random seed of 42. The same sample locations were used to extract NDVI and LST values for each of the four seasonal periods and the annual analysis. Seasonal and annual datasets were analyzed separately using paired NDVI and LST observations available for the respective periods. Pearson's correlation coefficient (r) was calculated to assess the strength and direction of the relationship between NDVI and LST, and the coefficient of determination (R^2) was calculated as the square of Pearson's correlation coefficient (r^2).

Software and Analytical Workflow

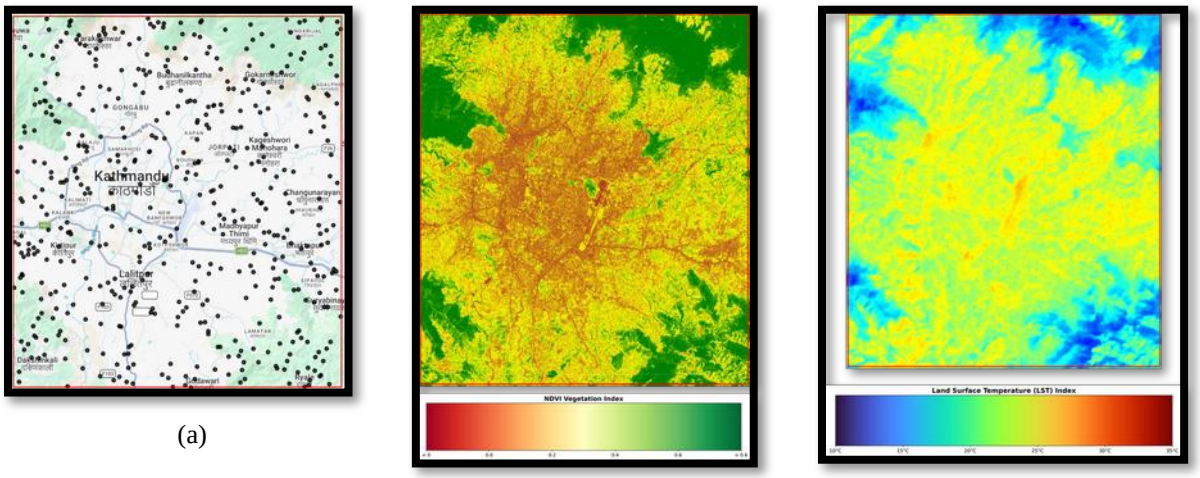
The satellite-image processing and calculations were performed using Google Earth Engine, a cloud-based platform for planetary-scale geospatial analysis (Gorelick .et al., 2017). It was used to filter satellite images, create median composites, derive NDVI and LST, perform random spatial sampling, calculate regional means, conduct correlation analysis, visualize data, and export to CSV. The exported sample datasets were used to create figures and perform other statistical analyzes for the study.

Results

Spatial Distribution of NDVI and LST

The relationship between NDVI and LST for the sampled locations in Kathmandu Valley in 2025 is shown in Figure 2. The scatter plot and fitted regression curve illustrate the overall relationship between vegetation greenness and surface temperature.

Figure 1



(a) (b) (c)

Figure 1
Spatial distribution of (a) the 500 sample points, (b) the NDVI, and (c)the LST across the study area in Kathmandu Valley in 2025.

Seasonal Variation in NDVI and LST

Figure 2 illustrates the seasonal distributions of LST and NDVI during 2025. These distributions provide a basis for comparing seasonal changes in LST and NDVI. The relationship between the two variables may differ across periods of the year.

Figure 2

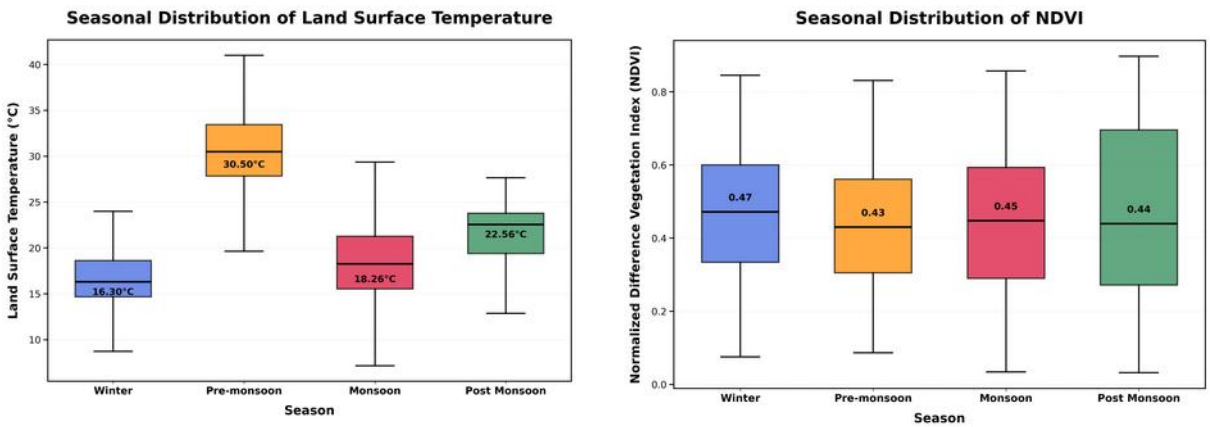


Figure 2
Seasonal variations in (a) LST and (b) NDVI across Kathmandu Valley in 2025.

Overall Relationship Between NDVI and LST

The annual analysis indicates a negative association between NDVI and LST across the study area (Figure 3). This pattern suggests that locations with greater vegetation greenness generally tended to have lower land surface temperatures. The strength of this association is summarized by the annual correlation results in Table 1.

Figure 3

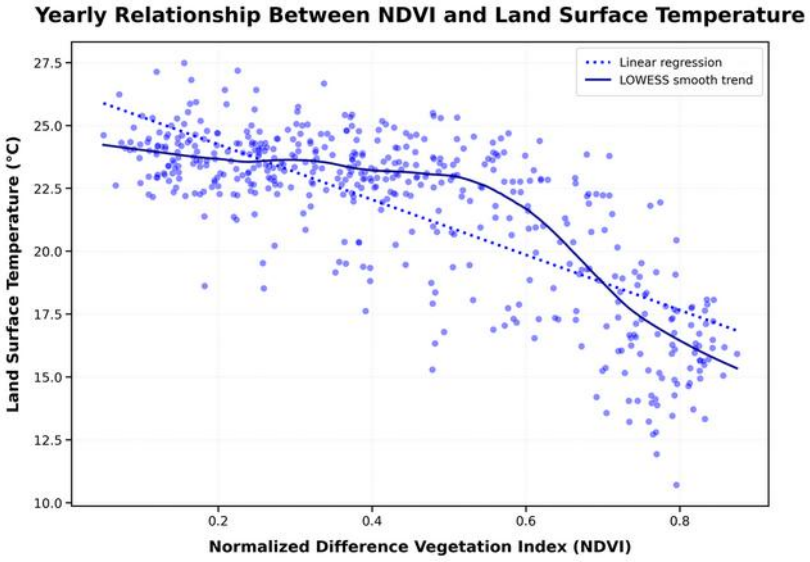


Figure 3
Relationship between NDVI and LST in Kathmandu Valley in 2025

Seasonal Relationship Between NDVI and LST

The seasonal correlation analysis revealed differences in the strength and direction of the NDVI–LST relationship (Figure 4; Table 1). The strongest negative association occurred during the pre-monsoon season, followed by the post-monsoon and winter seasons. In contrast, the monsoon

season showed a negligible positive correlation, indicating little linear association between the variables during this period.

Figure 4

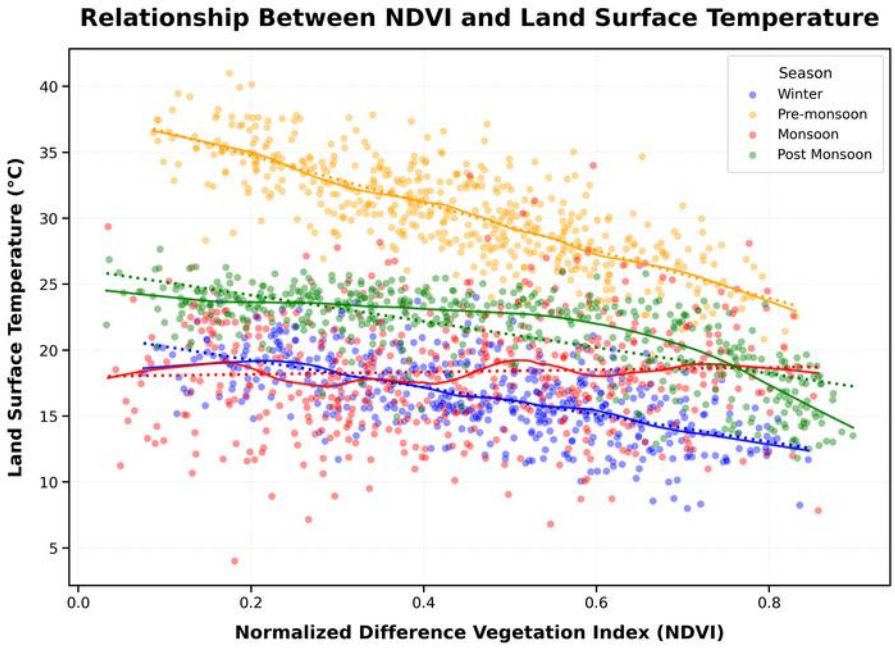


Figure 4

Relationship Between NDVI and LST Across Four Seasons in Kathmandu Valley, 2025

Table 1

Seasonal and Overall Correlation Between NDVI and Land Surface Temperature in Kathmandu Valley, 2025

Season	Period	Pearson's r	R^2	Interpretation
Winter	Jan–Feb 2025	−0.609	0.371	Moderate negative
Pre-monsoon	**Mar–May 2025**	**−0.776**	**0.602**	**Strong negative**
Monsoon	Jun–Sep 2025	+0.039	0.002	Weak
Post-monsoon	**Oct–Dec 2025**	**−0.714**	**0.509**	**Strong negative**
Overall	Jan–Dec 2025	−0.755	0.570	Strong negative

Note. Pearson's r represents the correlation coefficient, and R^2 represents the coefficient of determination. Values are rounded to three decimal places.

Discussion

Table 2

Comparison of Previous Studies with the Present Study

Study	Study area	Year / Period	Correlation (r)	R^2	Land type
Mishra et al. (2019)	Kathmandu Valley and adjacent areas	2000–2018	−0.65	0.45	Agriculture:−0.65; Forest: −0.30; Developed: −0.22

Sarif et al. (2020)	Kathmandu Valley	1988, 1998, 2008, 2018	−0.65 to −0.80	—	Overall
Karunaratne et al. (2022)	Kathmandu Valley	2000, 2013, 2020	—	0.696–0.781	Overall
Present Study	Kathmandu Valley	2025	−0.755	0.570	Overall

Note. (r) = Pearson's correlation coefficient; (R^2*) = coefficient of determination. A negative correlation indicates an inverse relationship between NDVI and LST. A dash (—) indicates that the statistic was not reported in the information presented. Values are based on the cited studies and the present study's analysis.*

The comparison shows that the present study also found a negative relationship between NDVI and LST, consistent with the general pattern reported in previous studies. The correlation coefficient of −0.75 indicates a relatively strong inverse relationship, while the R^2 value of 0.57 indicates that approximately 57% of the variation in LST is statistically associated with the fitted linear relationship with NDVI in the sampled data. However, differences in study periods, spatial coverage, and methods should be considered when comparing these results.

Limitations

The study is limited by the time period considered up to 2025, and therefore may not capture inter annual variability in vegetation conditions and temperature. Due to the limited availability of ground-based temperature data suitable for the current study, seasonal NDVI–LST relationships were analyzed using satellite-derived Landsat observations. However, cloud cover, especially during monsoon season, can limit the number of valid satellite observations. Moreover, the spatial resolution of satellite data might not be adequate to fully resolve the heterogeneous vegetation and built-up surfaces of Kathmandu Valley. Finally, the observed relationships indicate statistical associations rather than causation, as other environmental factors may also influence land surface temperature.

Conclusion

The study observed that the association of NDVI and LST varied significantly across the different seasons of 2025 in Kathmandu Valley. The general analysis indicated that the relationship between NDVI and LST was negative with pre-monsoon having the highest negative correlation followed by post-monsoon and winter. However, the linear relationship of the two variables was negligible during the monsoon season. The main contribution of the present study is the seasonal assessment of the NDVI-LST relationship, which shows that the seasonal variations of the NDVI-LST relationship cannot be well represented by the annual patterns only. However, the results suggest an association, not a causal relationship between NDVI and LST.

In the future studies, the analysis should be done for several years and the ground-based temperature observations should be included for validation purpose. In addition, other environmental factors should be taken into account to understand the seasonal variations of LST in Kathmandu Valley.

Acknowledgments

The author would like to express sincere gratitude to Asst. Prof. Dr. Babu Ram Tiwari and Prof. Dr. Khem Narayan Poudyal for their valuable guidance and support. The author also

acknowledges the Department of Applied Sciences and Chemical Engineering, Pulchowk Campus, Institute of Engineering, Tribhuvan University for the academic support and contribution in the completion of this study.

Funding

The author received no financial support for the research, authorship, or publication of this paper.

Conflict of Interest

The author declares no conflict of interest.

Data Availability

The data and code used in this study are available from the corresponding author upon reasonable request.

References

Aryal, A., Shakya, B. M., Maharjan, M., Talchabhadel, R., & Thapa, B. R. (2021). Evaluation of the land surface temperature using satellite images in Kathmandu Valley. Nepal Journal of Civil Engineering, 1(1), 1–10. https://civil.pcampus.edu.np/journal/index.php/njce/article/view/1.1-1

Bhandari, S., & Zhang, C. (2022). Urban green space prioritization to mitigate air pollution and the urban heat island effect in Kathmandu Metropolitan City, Nepal. Land, 11(11), Article 2074. https://doi.org/10.3390/land11112074

Bowler, D. E., Buyung-Ali, L., Knight, T. M., & Pullin, A. S. (2010). Urban greening to cool towns and cities: A systematic review of the empirical evidence. Landscape and Urban Planning, 97(3), 147–155. https://doi.org/10.1016/j.landurbplan.2010.05.006

Gill, S. E., Handley, J. F., Ennos, A. R., & Pauleit, S. (2007). Adapting cities for climate change: The role of green infrastructure. Built Environment, 33(1), 115–133. https://doi.org/10.2148/benv.33.1.115

Gorelick, N., Hancher, M., Dixon, M., Ilyushchenko, S., Thau, D., & Moore, R. (2017). Google Earth Engine: Planetary-scale geospatial analysis for everyone. Remote Sensing of Environment, 202, 18–27. https://doi.org/10.1016/j.rse.2017.06.031

Karunaratne, S., Athukorala, D., Murayama, Y., & Morimoto, T. (2022). Assessing surface urban heat island related to land use/land cover composition and pattern in the temperate mountain valley city of Kathmandu, Nepal. Remote Sensing, 14(16), Article 4047. https://doi.org/10.3390/rs14164047

Mishra, B., Sandifer, J., & Gyawali, B. R. (2019). Urban heat island in Kathmandu, Nepal: Evaluating relationship between NDVI and LST from 2000 to 2018. International Journal of Environment, 8(1), 17–29. https://doi.org/10.3126/ije.v8i1.22546

Oke, T. R. (1982). The energetic basis of the urban heat island. Quarterly Journal of the Royal Meteorological Society, 108(455), 1–24. https://doi.org/10.1002/qj.49710845502

Rouse, J. W., Haas, R. H., Schell, J. A., & Deering, D. W. (1974). Monitoring vegetation systems in the Great Plains with ERTS. In S. C. Freden, E. P. Mercanti, & M. A. Becker (Eds.), Third Earth Resources Technology Satellite-1 Symposium: Vol. 1. Technical

presentations, section A (NASA SP-351, pp. 309–317). National Aeronautics and Space Administration.

Sarif, M. O., Rimal, B., & Stork, N. E. (2020). Assessment of changes in land use/land cover and land surface temperatures and their impact on surface urban heat island phenomena in the Kathmandu Valley (1988–2018). ISPRS International Journal of Geo-Information, 9(12), Article 726. https://doi.org/10.3390/ijgi9120726

Sharma, I., Ueranantasun, A., & Tongkumchum, P. (2018). Modeling of satellite data to identify the seasonal patterns and trends of vegetation index in Kathmandu Valley, Nepal from 2000 to 2015. Jurnal Teknologi, 80(4), 125–133. https://doi.org/10.11113/jt.v80.11728

Voogt, J. A., & Oke, T. R. (2003). Thermal remote sensing of urban climates. Remote Sensing of Environment, 86(3), 370–384. https://doi.org/10.1016/S0034-4257(03)00079-8

Weng, Q. (2009). Thermal infrared remote sensing for urban climate and environmental studies: Methods, applications, and trends. ISPRS Journal of Photogrammetry and Remote Sensing, 64(4), 335–344. https://doi.org/10.1016/j.isprsjprs.2009.03.007

Climate Change Impact on Glacier and Snow Melt Runoff in Mugu Karnali Basin, Nepal

Suraj Khanal[1*], Tirtha Raj Adhikari[2]

[1]Department of Applied Sciences and Chemical Engineering, Pulchowk Campus, Lalitpur, Nepal
khanalsuraj9999@gmail.com
[2]Department of Hydrology and Meterology, Tribhuvan University
tirtha43@gmail.com
Corresponding Author:[*]khanalsuraj9999@gmail.com

Abstract

This study assessed the impact of climate change on glacier and snowmelt runoff in the Mugu Karnali Basin, Nepal, using a temperature-index degree-day model. Historical climate data for 2009–2023 were used to simulate rainfall runoff, snowmelt, glacier-melt runoff, and baseflow, with modelled snow-cover conditions evaluated against MODIS observations. Future climate and runoff were projected for 2015–2100 using the IPSL-CM6A-LR model under SSP2-4.5 and SSP5-8.5 scenarios. The model showed good agreement with MODIS snow-cover observations during calibration ($R^2 = 0.70$; RMSE = 3.85%). Results indicate that glacier melt, snowmelt, and baseflow are important components of basin runoff, while future climate change is expected to alter their relative contributions and the overall runoff regime. The study highlights the sensitivity of the Mugu Karnali Basin to climate change and provides useful information for understanding future water availability and supporting sustainable water-resource planning in the Himalayan region.

Keywords: Mugu Karnali Basin, Future climate and runoff, IPSL-CM6A-LR model, temperature-index degree-day model, climate change

1. Introduction:

Climate change is significantly affecting the hydrological processes of mountainous regions, particularly the Himalayan region, where snow and glaciers play an important role in maintaining river flows and freshwater availability (Carter et al., 2015). Rising temperatures and changes in precipitation influence snow accumulation, glacier mass balance, and the timing and magnitude of meltwater runoff. These changes can alter seasonal river discharge, potentially affecting downstream water resources, ecosystems, agriculture, and communities that depend on mountain-fed rivers. (Gao et al., 2018)

The Hindu Kush Himalayan region is particularly vulnerable to climate change because of its high dependence on snow and glacier melt and its complex topography (Hugonnet et al., 2021).Understanding these changes is challenging due to limited hydrological observations, especially in remote high-altitude catchments. Therefore, satellite-derived snow-cover information, climate datasets, and hydrological modelling provide important alternatives for assessing snow and glacier melt processes (Wulf et al., 2016). Temperature-based degree-day modelling offers a practical approach to estimating snowmelt and glacier melt and understanding their contributions to river runoff under changing climatic conditions (Kayastha & Kayastha, 2020).

In this context, the present study focuses on the Mugu Karnali Basin of western Nepal to investigate the impacts of climate change on snowmelt, glacier melt, and runoff. The study

evaluates historical climate and runoff conditions and examines future changes under the SSP2-4.5 and SSP5-8.5 climate scenarios. By integrating climate data, remote-sensing information, and a degree-day model, the research aims to understand how projected changes in temperature and precipitation may influence meltwater contributions, the hydrological regime, and future water-resource availability in the basin.

2. Literature Review / Related Work

The Himalayan region is an important source of freshwater, where seasonal snow and glaciers regulate river discharge. Rising temperatures associated with climate change are expected to alter snowfall, accelerate snow and glacier melting, and influence the seasonal distribution of runoff (Immerzeel et al., 2014). However, hydrological responses vary among basins depending on elevation, glacier coverage, and precipitation pattern.

Temperature-index models, particularly degree-day models, are widely used to estimate snow and glacier melt in data-scarce mountainous regions because of their relatively low data requirements.(Khadka et al., 2023) applied a temperature-index model in the Tamakoshi Basin, Nepal, to investigate climate change impacts on snowmelt, glacier melt, and runoff. Similarly, (Litt et al., 2019) highlighted the limitations of temperature-based melt models in representing complex glacier ablation processes. Remote sensing products, particularly MODIS snow-cover data, have also become important for monitoring snow-cover dynamics and evaluating hydrological model performance(Paudel & Andersen, 2011).

Climate change assessments using global climate models indicate that increasing temperatures and changing precipitation patterns may substantially alter Himalayan hydrology. (Muñoz-Sabater et al., 2021) highlighted the importance of climate projections and hydrological modelling for assessing future water availability in the region. Recent research in the Karnali Basin by (Pokhrel et al., 2026) further demonstrated the importance of snow storage in regulating streamflow and buffering drought conditions.

Despite these studies, basin-specific assessments of the individual contributions of rainfall, snowmelt, glacier melt, and baseflow remain important, particularly in data-scarce Himalayan catchments. Therefore, the present study investigates climate change impacts on glacier and snowmelt runoff in the Mugu Karnali Basin using an R-based degree-day model, MODIS snow-cover information, and bias-corrected IPSL-CM6A-LR climate projections under SSP2-4.5 and SSP5-8.5 scenarios for 2015–2100. The study evaluates changes in individual runoff components to understand potential future hydrological responses.

3. Materials and Methods

3.1 Study Area

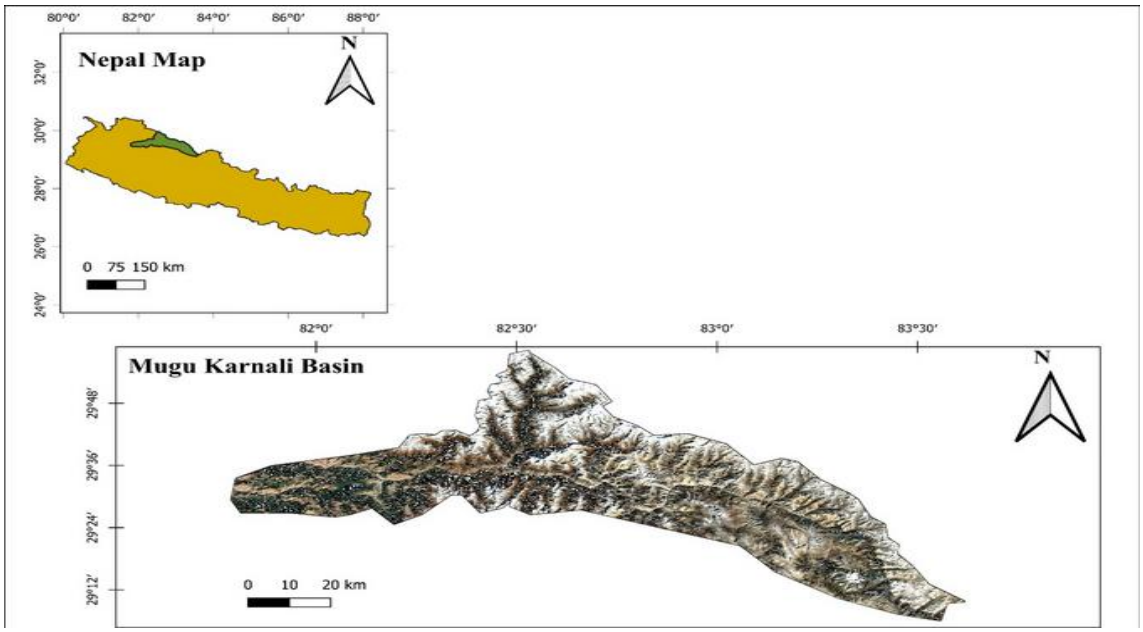


Figure 1: Overview of study area and its location

The major characteristics of the study area are summarized below:

Location: Northwestern Nepal

River system: Karnali River Basin

Basin area: Approximately 5,400 km²

Elevation: Approximately 1,100–6,300 m above sea level

Terrain: Predominantly mountainous with a strong elevation gradient

3.2 Data Sources

Table 1: Datasets used in the study

Dataset	Source	Resolution	Purpose
Digital Elevation Model (DEM)	SRTM/HydroSHEDS	~30 m	Elevation representation and temperature correction
Glacier inventory	Randolph Glacier Inventory (RGI)	Vector	Glacier extent and distribution
Ice thickness	Glacier ice-thickness dataset	Raster	Estimation of glacier ice melt
Air temperature (2009–2023)	ERA5-Land	0.1° / daily	Temperature input for the Degree-Day Model
Precipitation (2009–2023)	ERA5-Land	0.1° / daily	Snow accumulation and rainfall input
MODIS MOD10A2 (2009–2023)	NASA	500 m / 8-day	Derivation of observed SCA and SCF
Historical and future climate data (2009–	IPSL-CM6A-LR (CMIP6)	Model dependent	Climate change impact assessment

2100)			

3.3 Data Processing and Model Development:

Daily temperature and precipitation datasets were processed for historical (2009–2023) and future (2015–2100) simulations. DEM and glacier inventory data were used to characterize basin topography and glacier distribution, while MODIS-derived snow-cover data were used for model evaluation. Future climate data from the IPSL-CM6A-LR model under SSP2-4.5 and SSP5-8.5 scenarios were bias-corrected using Quantile Delta Mapping (QDM).

A temperature-index-based degree-day model was developed in R to simulate snow accumulation, snowmelt, glacier melt, and runoff generation. Precipitation was partitioned into rainfall and snowfall using a 0°C threshold, while snow and glacier melt were estimated using temperature-dependent degree-day factors. The model also incorporated soil and groundwater storage to represent delayed runoff and baseflow contributions. Finally, rainfall runoff, direct snowmelt runoff, glacier melt, and baseflow were combined to estimate total basin runoff under historical and future climate conditions.

The resulting runoff components are summed and converted from runoff depth to stream discharge.

1. Rainfall and snowfall partitioning

Precipitation is separated into rainfall and snowfall based on the temperature threshold:

$$P_r = \quad (1)$$

And,

$$P_s = \quad (2)$$

Where, P is total precipitation, P_r is rainfall, P_s is snowfall, and T_{sr} is the snow–rain temperature threshold.

In the model, T_{sr}= 0°C. Therefore, precipitation occurring when T_t> 0°C is treated as rainfall, whereas precipitation occurring at or below 0° C is treated as snowfall.

The partitioning ensures that the total precipitation is conserved:

$P_t = P_{r,t} + P_{s,t}$

This partitioning is important because rainfall contributes directly to soil infiltration and runoff, whereas snowfall is first stored as snowpack and subsequently released through snowmelt.

2. Snow accumulation and snowmelt

Snowfall is accumulated as snow water equivalent (SWE):

$$SWE_t=SWE_{t-1}+P_s-Ms \quad (3)$$

Snowmelt is calculated using the degree-day equation:

$$M_{s,p}=DDF_s(T-T_m) \quad (4)$$

when $T>T_m$, otherwise $M_{s,p}=0$.

The actual snowmelt cannot exceed the available SWE:

$$Ms=\min(M_{s,p},SWE) \quad (5)$$

Where, DDF_s is the snow degree-day factor and T_m is the melt threshold temperature.

This equation represents the daily snow water balance. Snowfall increases the snowpack, while snowmelt decreases it. Thus, the equation maintains the temporal storage of snow before it becomes available as liquid water.

The initial snow water equivalent used in the model is SWE_0=1 mm.

3. Glacier ice melt

Glacier melt is also calculated using the degree-day approach. Glacier ice melt is generated when the air temperature exceeds the melt threshold and when the glacier surface is not covered by snow:

$$M_g=DDF_g(T-T_m) \quad (6)$$

when $T>T_m$, otherwise M_g =0.

The glacier melt is converted to a basin-equivalent runoff depth using:

$$R_g \quad (7)$$

Where, $M_{g,i}$ is glacier melt at cell i, A_i is the glacier cell area, and A_b is the total basin area.

4. Rainfall infiltration and rainfall runoff

Rainfall first enters the soil according to the available soil storage and infiltration capacity:

$$I_r=\min(P_r, I_{cap}) \quad (8)$$

The remaining rainfall becomes rainfall runoff:

$$R_r=P_r-I_r \quad (9)$$

5. Snowmelt infiltration and runoff

Snowmelt can also infiltrate into the soil:

$$Is=\min (M_s, I_{cap,rem}) \quad (10)$$

The remaining snowmelt becomes direct snowmelt runoff:

$$R_s=M_s-I_s \quad (11)$$

6. Soil drainage

Water stored in the soil above field capacity contributes to groundwater recharge:

$$D_s=k_p(S-S_{FC}) \quad (12)$$

where D_s is soil drainage, k_p is the percolation coefficient, S is soil water storage, and $S_{FC}$is soil water storage at field capacity.

7. Groundwater and baseflow

Soil drainage is added to:

$$G_t=G_{t-1}+D_s-R_b \quad (13)$$

Baseflow is calculated from groundwater storage as:

$$R_b=k_gG_t \quad (14)$$

Where, k_g is the groundwater recession coefficient.

If groundwater storage exceeds its maximum capacity, the excess is treated as additional quick runoff.

8. Total runoff

The total basin runoff is obtained by adding the four major runoff components:

$$R_{total} = R_r + R_s + R_g + R_b \quad (15)$$

where:

R_r = rainfall runoff

R_s = snowmelt runoff

R_g = glacier melt runoff

R_b = baseflow

9. Conversion of runoff to discharge

Finally, the total runoff depth is converted into stream discharge:

(16)

where:

Q = discharge (m^3/s)

R_{total} = total runoff (mm/day)

A_b = basin area (km^2)

3.4 Model Calibration and Validation:

The degree-day model was calibrated using MODIS-derived snow-cover fraction (SCF) data for the period 2009–2018 to assess its ability to represent seasonal snow-cover dynamics. Model parameters, including snow and glacier degree-day factors and temperature thresholds, were selected to obtain reasonable agreement between simulated and satellite-derived snow-cover conditions. Model evaluation was performed using the coefficient of determination (R^2), root mean square error (RMSE), mean absolute error (MAE), and mean bias error (MBE).

Table 2: Calibrated parameters, search ranges, fitted values and sources

Parameter	**Description**	**Calibration range**	**Fitted value**	**Basis/source**
T threshold	Melt threshold temperature	-2.0 to 1.0 °C	-2 °C	Hock (2003)
T snow- rain	Snow–rain separation temperature	0.0 to 2.0 °C	0 °C	High-mountain snow modelling literature
DDF Snow	Snow degree-day factor	2.0-8.0 mm $°C^{-1}$ day^{-1}	7mm $°C^{-1}$ day^{-1}	Hock (2003); Braithwaite (2008)
DDF Ice	Ice degree-day factor	2.0-10.0 mm $°C^{-1}$ day^{-1}	9°mm$°C^{-1}$$day^{-1}$	Hock (2003); Himalayan studies

3.5 Bias Correction of Climate Model Data:

Future temperature and precipitation projections from the IPSL-CM6A-LR climate model were bias-corrected using the Quantile Delta Mapping (QDM) method to reduce systematic biases in raw climate simulations. The correction was performed using historical reference data from ERA5 and corresponding historical climate model outputs. QDM preserves projected changes in climate variables while adjusting their statistical distributions to better match the reference climate. The bias-corrected daily temperature and precipitation data were subsequently used to drive the degree-day model under SSP2-4.5 and SSP5-8.5 scenarios for the period 2015–2100.

Temperature correction was expressed as:

$$T_{bc}=T_{m,f}+[Q_{o,h}(p)-Q_{m,h}(p)] \quad (17)$$

Precipitation correction was expressed as:

$$P_{bc}=P_{m,f} \ * \quad (18)$$

Where, T_{bc} and P_{bc} represent bias-corrected temperature and precipitation, respectively; $Q_{o,h}$ and $Q_{m,h}$ denote the observed and modelled historical quantiles and $T_{m,f}$ and $P_{m,f}$ represent future model projections.

3.6 Future Climate Scenario Analysis:

Future hydrological simulations were conducted for the period 2015–2100 using bias-corrected daily temperature and precipitation projections from the IPSL-CM6A-LR climate model under two emission scenarios: SSP2-4.5 and SSP5-8.5. The simulations were performed using the developed degree-day model with consistent model parameters to assess changes in snow accumulation, snowmelt, glacier melt, rainfall runoff, and baseflow.

The future period was divided into baseline (2015–2023), near-future (2029–2052), mid-future (2053–2076), and far-future (2077–2100) periods. The simulated results were compared to identify changes in climatic conditions, individual runoff components, and total discharge under both scenarios. This analysis provided insights into the potential long-term effects of climate change on the hydrological regime and water availability of the Mugu Karnali Basin.

Methodological Framework:

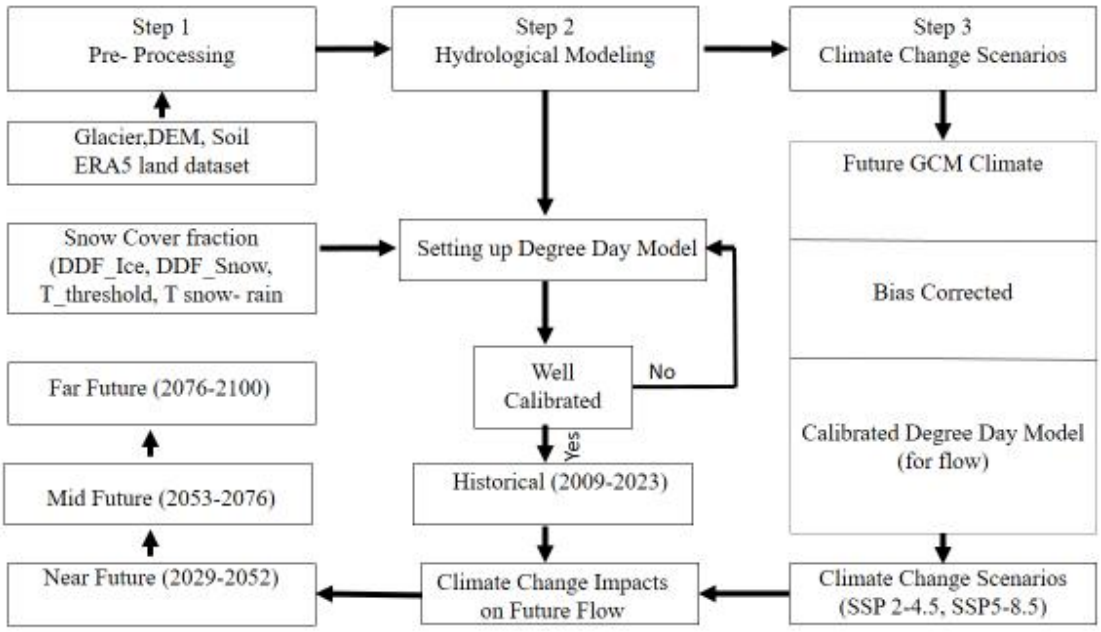


Figure 2: Methodological Framework

4. Results

4.1 Historical Climate Characteristics:

A. Temperature:

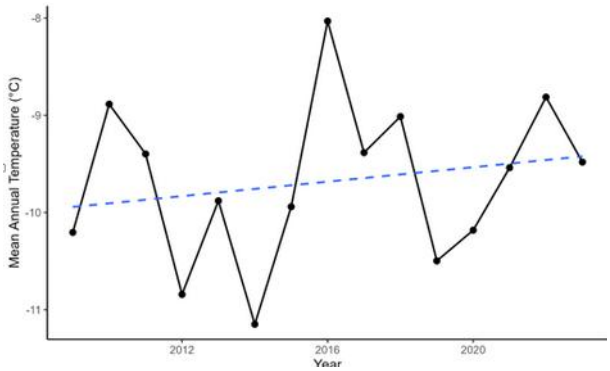
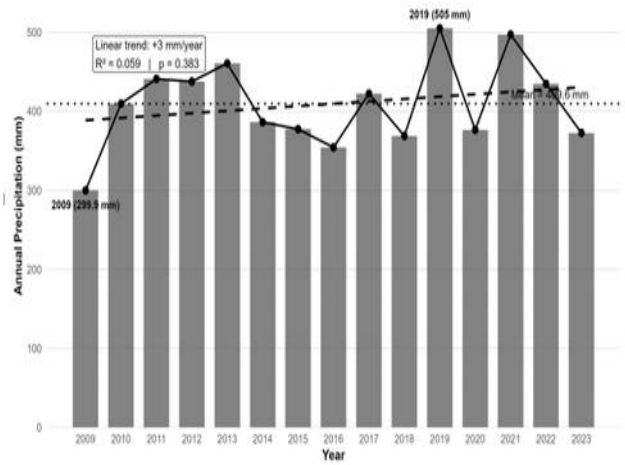


Figure 3: Historical annual temperature

The mean annual temperature during 2009-2023 showed an increasing tendency. The Mann–Kendall test produced a positive Kendall's tau of 0.143, indicating an overall upward direction in the temperature series. The Sen's slope was estimated at 0.049 °C year^{-1}, equivalent to approximately 0.49 °C decade^{-1}. However, the trend was not statistically significant at the 5% significance level, with a p-value of 0.458 ($p > 0.05$). Therefore, although the historical temperature series indicates a warming tendency, the available 2009–2023 record does not provide sufficient statistical evidence to confirm a significant long-term temperature trend.



B. Precipitation:

The annual precipitation series derived from ERA5-Land for 2009–2023 exhibited a weak increasing tendency. The Mann–Kendall test resulted in a Kendall's tau of

0.029 with a p-value of 0.882, indicating that the observed increasing tendency was not statistically significant at the 5% significance level. The Sen's slope was estimated at 1.814 mm year^{-1}, corresponding to approximately 18.14 mm decade^{-1}. Therefore, although the precipitation series showed a slight upward tendency during the study period, the statistical analysis did not provide sufficient evidence of a significant long-term change in annual precipitation

4.2 Snow Cover and Model Performance:

Table 3: Performance metric from calibration of model

Metric	Result	Interpretation
R^2	0.702	Reasonably strong agreement/ability to reproduce SCF variability
RMSE	3.85%	Small overall prediction error
MAE	3.26%	Model differs from MODIS by ~3.26 percentage points on average
MBE	−0.49%	Very small overall underestimation

Table 4: Fitted values after calibration

Calibration period	DDF snow	DDF ice	T threshold	T snow rain	Lapse rate
2009- 2018	7	9	-2	0	0.0065

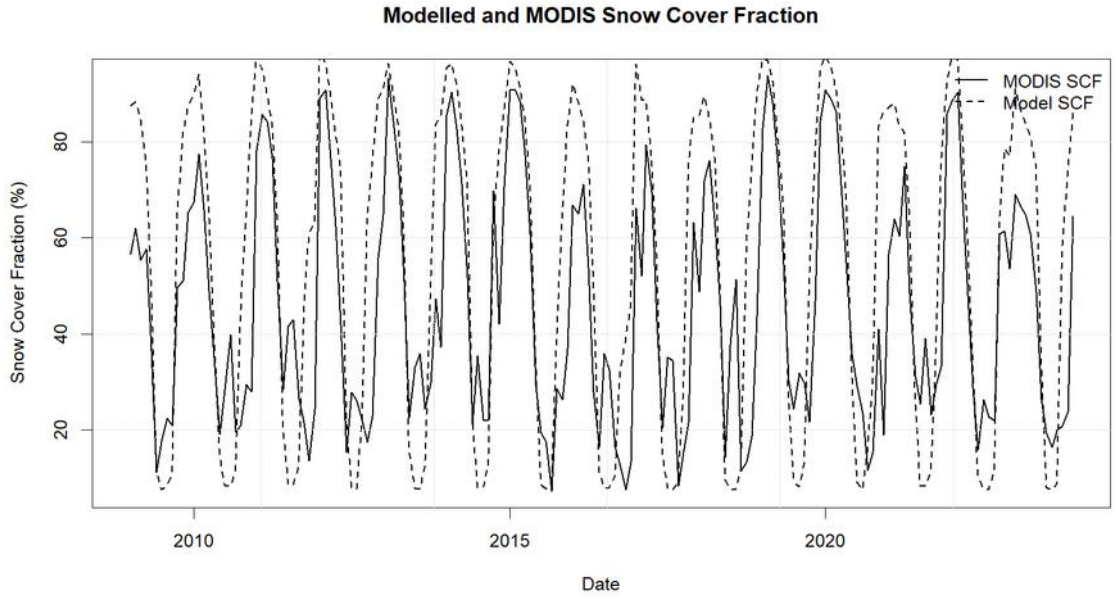


Figure 5: Comparison of MODIS and modeled SCF

4.3 Historical Discharge:

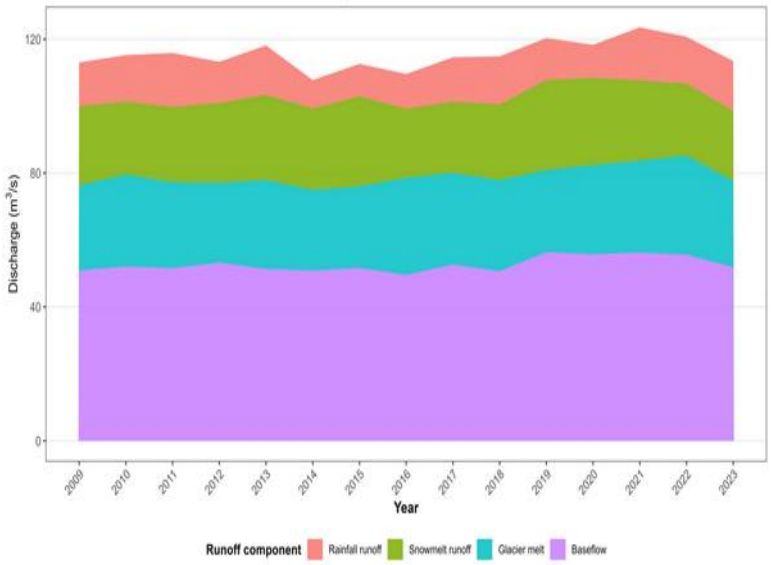


Figure 6: Mean discharge and its components

Figure 6 shows the historical discharge for study period of 2009-2023 for Snowmelt, glaciermelt, rainfall runoff and baseflow components

4.4 Future Climate Projections:

- Future temperature:

Table 5: Future temperature under SSP2-4.5 and SSP5-8.5

Scenario	Future Period	Start Year	End Year	Mean Temperature	Change from Baseline
SSP2-4.5	Baseline (2015-2023)	2015	2023	-7.98	0
SSP2-4.5	Near Future (2029-2052)	2029	2052	-6.82	1.16
SSP2-4.5	Mid Future (2053-2076)	2053	2076	-5.83	2.14
SSP2-4.5	Far Future (2077-2100)	2077	2100	-4.77	3.21
SSP 5-8.5	Baseline (2015-2023)	2015	2023	-7.18	0
SSP 5-8.5	Near Future (2029-2052)	2029	2052	-5.59	1.58
SSP 5-8.5	Mid Future (2053-2076)	2053	2076	-2.95	4.22
SSP 5-8.5	Far Future (2077-2100)	2077	2100	0.44	7.62

Table 6: Future precipitation under SSP 2-4.5 and SSP 5-8.5

Scenario	Period	Mean Annual Precipitation mm	Change from Baseline (mm)	Change from Baseline (%)
SSP2-4.5	Baseline 2015-2023	441.29	0	0
SSP2-4.5	Near	418.65	-29.16	-6.51

	2029-2052			
SSP2-4.5	Mid 2053-2076	463.27	21.98	4.98
SSP2-4.5	Far 2077-2100	564.85	123.56	27.99
SSP5-8.5	Baseline 2015-2023	390.98	0	0
SSP5-8.5	Near 2029-2052	416.34	25.36	7.84
SSP5-8.5	Mid 2053-2076	664.12	273.14	69.86
SSP5-8.5	Far 2077-2100	862.85	471.86	120.68

4.5 Future Discharge:

Table 7: Future Discharge under SSP 2-4.5

Period	Mean Discharge	Change from baseline	% change from baseline
Baseline	115.81	0	0
Near Future	123.25	7.44	6.42
Mid Future	131.93	16.12	13.92
Far Future	141.06	25.24	21.80

Table 8: Future Discharge under SSP 5-8.5

Period	Mean Discharge	Change from baseline	% change from baseline
Baseline	102.33	0	0
Near Future	113.91	11.58	11.31
Mid Future	147.29	44.96	43.94
Far Future	183.06	80.73	78.89

Under SSP2-4.5, mean discharge is projected to increase gradually from 115.81 m^3/s during the baseline period to 141.06 m^3/s in the far future, representing an overall increase of 21.80%.

Under SSP5-8.5, the increase is considerably higher, with mean discharge rising from 102.33 m^3/s to 183.07 m^3/s by the far future, representing a 78.90% increase relative to the baseline.

Overall, both scenarios indicate an increasing trend in future discharge, with SSP5-8.5 showing a substantially stronger hydrological response than SSP2-4.5, particularly during the mid- and far-future periods

5. Discussion

The projected discharge results indicate an increasing trend in streamflow under both climate change scenarios, with the magnitude of increase becoming more pronounced under the higher-emission scenario. Under SSP2-4.5, mean discharge increases from 115.81 m^3/s during the baseline period to 123.26 m^3/s in the near future, 131.94 m^3/s in the mid-future, and 141.06 m^3/s in the far future. This represents an overall increase of 21.80% by the end of the century. In comparison, SSP5-8.5 shows a much stronger increase, with mean discharge rising from 102.33 m^3/s during the baseline period to 113.91 m^3/s in the near future, 147.30 m^3/s in the mid-future, and 183.07 m^3/s in the far future, corresponding to an overall increase of 78.90%.

The substantially higher discharge projected under SSP5-8.5 suggests that stronger future warming could considerably influence the hydrological response of the Mugu Karnali Basin.

Rising temperatures can accelerate snow and glacier melt, while changes in precipitation patterns may further influence runoff generation. The increasing discharge may also reflect changes in groundwater contributions and the seasonal availability of meltwater. The difference between the two scenarios becomes particularly evident during the mid- and far-future periods, highlighting the importance of future emission pathways in determining the basin's hydrological response.

The results suggest that climate change may significantly alter the future runoff regime of the Mugu Karnali Basin, particularly under SSP5-8.5. The projected increase in discharge indicates the potential for greater water availability in terms of annual flow; however, it may also increase the risk of high-flow events and associated flood hazards. These changes highlight the importance of considering future climate scenarios in water resource planning and hydrological risk management in the basin.

7. Limitations

1. Limited availability of reliable ground-based meteorological and hydrological observations in the remote and high-altitude areas of the Mugu Karnali Basin.
2. The use of reanalysis, satellite, and climate-model datasets introduces uncertainties related to data resolution, quality, and representation of complex Himalayan terrain.
3. Future climate projections and hydrological simulations are subject to uncertainties associated with climate models, scenarios, and model parameterization.

6. Conclusion

1. The projected discharge indicates an increasing trend under both climate change scenarios. Mean discharge is projected to increase by 21.80% under SSP2-4.5 and 78.90% under SSP5-8.5 by the far-future period (2077–2100), indicating a stronger hydrological response under the high-emission scenario.

2. The projected changes in discharge highlight the potential influence of future temperature and precipitation changes on snowmelt, glacier melt, and overall runoff generation in the Mugu Karnali Basin. The magnitude of change becomes more pronounced during the mid- and far-future periods, particularly under SSP5-8.5.

3. The increasing discharge suggests potential changes in future water availability and hydrological conditions in the basin. Therefore, climate change considerations should be incorporated into long-term water resource planning and sustainable management of the Mugu Karnali Basin

References

Carter, J. G., Cavan, G., Connelly, A., Guy, S., Handley, J., & Kazmierczak, A. (2015). Climate change and the city: Building capacity for urban adaptation. *Progress in Planning, 95*, 1–66. https://doi.org/10.1016/j.progress.2013.08.001

Gao, H., Li, H., Duan, Z., Ren, Z., Meng, X., & Pan, X. (2018). Modelling glacier variation and its impact on water resource in the Urumqi Glacier No. 1 in Central Asia. *Science of The Total Environment, 644*, 1160–1170. https://doi.org/10.1016/j.scitotenv.2018.07.004

Hugonnet, R., McNabb, R., Berthier, E., Menounos, B., Nuth, C., Girod, L., Farinotti, D., Huss, M., Dussaillant, I., Brun, F., & Kääb, A. (2021). Accelerated global glacier mass loss in

the early twenty-first century. *Nature*, *592*(7856), 726–731. https://doi.org/10.1038/s41586-021-03436-z

Immerzeel, W. W., Petersen, L., Ragettli, S., & Pellicciotti, F. (2014). The importance of observed gradients of air temperature and precipitation for modeling runoff from a glacierized watershed in the Nepalese Himalayas. *Water Resources Research*, *50*(3), 2212–2226. https://doi.org/10.1002/2013WR014506

Kayastha, R. B., & Kayastha, R. (2020). Glacio-Hydrological Degree-Day Model (GDM) Useful for the Himalayan River Basins. In A. P. Dimri, B. Bookhagen, M. Stoffel, & T. Yasunari (Eds.), *Himalayan Weather and Climate and their Impact on the Environment* (pp. 379–398). Springer International Publishing. https://doi.org/10.1007/978-3-030-29684-1_19

Khadka, N., Chen, X., Sharma, S., & Shrestha, B. (2023). Climate change and its impacts on glaciers and glacial lakes in Nepal Himalayas. *Regional Environmental Change*, *23*(4), 143. https://doi.org/10.1007/s10113-023-02142-y

Litt, M., Shea, J., Wagnon, P., Steiner, J., Koch, I., Stigter, E., & Immerzeel, W. (2019). Glacier ablation and temperature indexed melt models in the Nepalese Himalaya. *Scientific Reports*, *9*(1), 5264. https://doi.org/10.1038/s41598-019-41657-5

Muñoz-Sabater, J., Dutra, E., Agustí-Panareda, A., Albergel, C., Arduini, G., Balsamo, G., Boussetta, S., Choulga, M., Harrigan, S., Hersbach, H., Martens, B., Miralles, D. G., Piles, M., Rodríguez-Fernández, N. J., Zsoter, E., Buontempo, C., & Thépaut, J.-N. (2021). ERA5-Land: A state-of-the-art global reanalysis dataset for land applications. *Earth System Science Data*, *13*(9), 4349–4383. https://doi.org/10.5194/essd-13-4349-2021

Paudel, K. P., & Andersen, P. (2011). Monitoring snow cover variability in an agropastoral area in the Trans Himalayan region of Nepal using MODIS data with improved cloud removal methodology. *Remote Sensing of Environment*, *115*(5), 1234–1246. https://doi.org/10.1016/j.rse.2011.01.006

Pokhrel, P., Griffioen, J., Bogaard, T. A., Kraaijenbrink, P. D. A., Fiddes, J., & Immerzeel, W. W. (2026). Upstream hydrology and the importance of snowmelt in buffering droughts in the Karnali basin in Nepal. *Frontiers in Water*, *7*, 1720178. https://doi.org/10.3389/frwa.2025.1720178

Wulf, H., Bookhagen, B., & Scherler, D. (2016). Differentiating between rain, snow, and glacier contributions to river discharge in the western Himalaya using remote-sensing data and distributed hydrological modeling. *Advances in Water Resources*, *88*, 152–169. https://doi.org/10.1016/j.advwatres.2015.12.004

Estimation of Solar Energy Using Sunshine Hours and Temperature for Climate Resilient Energy Planning at Dhunibeshi, Dhading, Nepal

Arjun Gautam[1*], Khem Narayan Poudyal[2], Babu Ram Tiwari[2]

[1]M.Sc. Climate Change and Development, Institute of Engineering, Pulchowk Campus, Tribhuvan University, Lalitpur, Nepal

[2]Department of Applied Sciences and Chemical Engineering, Institute of Engineering, Pulchowk Campus, Tribhuvan University, Lalitpur, Nepal

gautamarjun2014@gmail.com; khem@ioe.edu.np; baburam.tiwari@pcampus.edu.np

[*]Corresponding author: gautamarjun2014@gmail.com

Abstract

Nepal is a landlocked Himalayan country with complex terrain, where climate-induced disasters such as floods and landslides occur frequently and place its hydropower infrastructure at serious risk. However, Nepal receives abundant solar exposure, with an estimated 300 sunny days per year, an average sunshine duration of 6.8 hours per day and solar insolation ranging from 3.6–6.2 kWh/m²/day, which indicates a high potential for solar energy in different parts of the country. This study estimates the solar energy potential of mid-hill Nepal at Dhunibeshi, Dhading. Hourly radiation and sunshine records and daily temperature records for 2020–2025 (1,806 valid days) were used in a sunshine-based model (Ångström–Prescott) and a temperature-based model (Hargreaves–Samani). Regression coefficients were derived by the least squares method and then applied to estimate the solar energy potential of the site. The Ångström–Prescott model gave coefficients a = 0.242 and b = 0.417, and the Hargreaves–Samani model gave c = 0.135. The measured mean daily radiation was 14.34 MJ/m²/day, while the two models estimated 14.20 and 14.51 MJ/m²/day, respectively. Compared with the measured values, the coefficient of determination was $R^2 = 0.79$ for the Ångström–Prescott model and $R^2 = 0.55$ for the Hargreaves–Samani model, with a root mean square error (RMSE) of 2.35 and 3.44 MJ/m²/day. These findings show that the Ångström–Prescott model is more accurate than the Hargreaves–Samani model because of the direct effect of sunshine hours. The model can therefore be used to estimate the solar energy potential in areas of Nepal with similar climatic conditions.

Keywords: Solar energy potential, sunshine hours, temperature, empirical models, regression analysis

Introduction

Nepal has favorable conditions for solar energy. It lies at approximately 27.5° N latitude, within the global solar belt, and receives around 300 sunny days a year (Poudyal, 2015) with an average of 6.8 hours of sunshine each day (Water and Energy Commission Secretariat [WECS], 2010). Daily global radiation across the country has been reported to range from 3.6 to 6.2 kWh/m²/day (Poudyal, 2015). Even so, solar planning needs radiation data from the actual site, and these are hard to find, because radiation instruments are costly to buy and maintain and few stations have them (Dhakal et al., 2020; Joshi et al., 2022). Empirical estimation models are the usual way to fill this gap.

Empirical models are broadly classified into two main categories. Sunshine-based models link the clearness index to the fraction of the day with bright sunshine, a relation first given by Ångström (1924) and later modified by Prescott (1940). Temperature-based models treat the

daily temperature range as an indicator of cloudiness, and the Hargreaves–Samani model is the best known of them (Hargreaves & Samani, 1985). In Nepal, sunshine-based coefficients have been calibrated at fifteen stations (Joshi et al., 2022), temperature-based and machine-learning models have been compared at Biratnagar Airport (Dhakal et al., 2020), and daily radiation estimation has been examined more broadly (Poudyal et al., 2013). Dhunibeshi is one of the stations in Joshi et al. (2022), but that study did not compare sunshine-based and temperature-based approaches there.

This paper fills that gap. Its objectives are (a) to calibrate the Ångström–Prescott and Hargreaves–Samani models for Dhunibeshi using locally measured meteorological data; (b) to estimate global solar radiation using meteorological parameters.

Literature Review / Related Work

Sunshine based estimation

Ångström (1924) established a linear relationship between the ratio of global solar radiation to clear-sky radiation and relative sunshine duration. Prescott (1940) later modified this relationship by replacing clear-sky radiation with extraterrestrial solar radiation, which can be calculated using geographical latitude and the day of the year. The resulting Ångström–Prescott equation remains the most widely used sunshine-based relation and has been reviewed extensively (Akinoğlu, 1991). Its intercept a gives the share of extraterrestrial radiation that still reaches the ground under a fully overcast sky, while $a + b$ is close to the clearness of a completely clear sky (Poudyal, 2015). Since many stations record sunshine duration routinely, the model is a practical way to extend radiation coverage, and coefficients have even been derived for entire countries such as India (Srivastava & Pandey, 2013).

Temperature based estimation

Where sunshine records are unavailable, air temperature is the most common input, because maximum and minimum temperatures are recorded at nearly all weather stations. Hargreaves and Samani (1985) related the clearness index to the square root of the daily temperature range through one empirical coefficient. Clear days have higher maximum and lower minimum temperatures than cloudy days, so the range acts as a proxy for cloud cover. The method was originally developed to estimate evapotranspiration (Hargreaves & Samani, 1985), and the Food and Agriculture Organization (FAO) guidelines (FAO-56) use the same form with a coefficient of 0.16 for interior and 0.19 for coastal sites (Allen et al., 1998). Later work added humidity to the model (Valiantzas, 2018) and calibrated it over space and time (Samani et al., 2011). Its accuracy in mountainous terrain, where local circulation and terrain strongly affect temperature, is less well established.

Solar radiation studies in Nepal

Joshi et al. (2022) fitted Ångström–Prescott coefficients for fifteen stations across Nepal and reported pooled values of a = 0.239 and b = 0.508, giving a root mean square error (RMSE) of 1.958 MJ/m²/day, a mean bias error (MBE) of −0.018 and a correlation coefficient (r) of 0.909. For Dhunibeshi itself (1085 m above sea level) the same study gave a = 0.235 and b = 0.432, with a measured annual mean of 14.17 MJ/m²/day compared with a modelled 14.009. At Biratnagar Airport, Dhakal et al. (2020) tested six temperature-based empirical models against an artificial neural network and five other machine-learning methods. The best of the temperature-based models was a multi-variable formulation (coefficient of determination R^2 = 0.7498, RMSE

= 2.0162 MJ/m²/day), whereas stepwise linear regression and a neural network, both of which also drew on sunshine duration, precipitation and humidity, reached R^2 values of 0.8870 and 0.8446. Poudyal (2015) recorded annual mean insolation of 4.21, 4.87, 3.70 and 4.69 kWh/m²/day at Biratnagar, Pokhara, Lukla and Kathmandu during 2009–2010, and Poudyal et al. (2013) looked at how daily global radiation can be estimated from Nepali measurements. Joshi et al. (2021) used six years of radiation data from the Kathmandu Valley to compare four empirical models based on sunshine hours, temperature range and relative humidity; the best of them, which combined all three inputs, reached R^2 = 0.792 and RMSE = 1.405 MJ/m²/day. Poudyal (2016) tested a modified Ångström formula at Pokhara in the Himalayan region, and Saud et al. (2023) used the Ångström and Gopinathan models with sunshine hours and temperature data from highland Nepal.

Materials and Methods

Study site and data

Dhunibeshi is located in Dhading District, Bagmati Province,Nepal, at 27.7229° N, 85.1643° E (Figure 1), and the station stands at an elevation of 1085 m (Joshi et al., 2022). Hourly global solar radiation (W/m²) and hourly sunshine duration (h) were obtained from the Department of Hydrology and Meteorology (DHM), Government of Nepal, together with daily maximum and minimum air temperature (°C). The record spans February 2020 to November 2025.

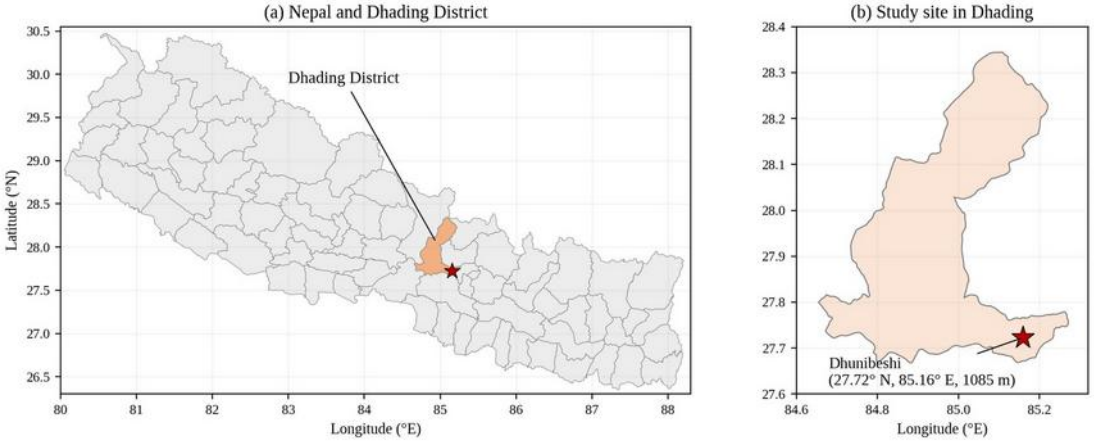


Figure 1

Map of Nepal Showing Dhading District and the Dhunibeshi Study Site

(a) Location of Dhading District in Nepal. (b) Location of the Dhunibeshi station (27.72° N, 85.16° E, 1085 m) within Dhading District.

Daily global solar radiation H (MJ/m²/day) was obtained by summing the hourly irradiance values over each day and multiplying by 3600 s h^{-1} divided by 10^6. Daily sunshine duration n (h) is the sum of the hourly values. The daily mean temperature was computed as $T_a = (T_{max} + T_{min})/2$ and the diurnal range as $\Delta T = T_{max} - T_{min}$.

Quality control

Three rules were applied. First, months in which the sunshine sensor was faulty (the monthly sunshine sum was zero although radiation data were present; August–November 2023) were

excluded. Second, months with less than 80% hourly completeness were excluded. Third, individual days with fewer than 20 of 24 hourly records were excluded. After these steps and merging with the temperature record, 1,806 valid days from 61 calendar months remained and formed the data set. Excluded months were spread across all seasons, and every calendar month retained at least four of the six years, so the retained data are not biased toward any season.

Extraterrestrial radiation and day length

Extraterrestrial radiation H_0 and maximum possible sunshine duration N were computed from the standard astronomical relations given by Duffie and Beckman (2013), using the site latitude φ and the day of the year n_d:

(1)

(2)

(3)

(4)

(5)

where H_0 is the extraterrestrial radiation (MJ/m²/day), and the factor 10^{-6} converts J/m²/day to MJ/m²/day; I_{sc} = 1367 W/m² is the solar constant; E_0 is the eccentricity correction factor; n_d is the day of the year (1 January = 1; 31 December = 365); φ is the latitude of the site (27.7229° N); δ is the solar declination; ω_s is the sunset hour angle (in radians in Eq. 1 and in degrees in Eq. 5); and N is the maximum possible sunshine duration, or day length (h).

Empirical models

Two empirical models were used. They are listed in Table 1 with their inputs and the relation between the clearness index and the predictors.

Table 1

List of Models Used for the Estimation of Global Solar Radiation

Model	Symbol	Inputs	Relation
Ångström–Prescott (Ångström, 1924; Prescott, 1940)	AP	n, N, H_0	$H/H_0 = a + b(n/N)$
Hargreaves–Samani (Hargreaves & Samani, 1985)	HS	T_{max}, T_{min}, H_0	$H/H_0 = c\sqrt{(T_{max} - T_{min})}$

Note. n = sunshine duration; N = maximum possible sunshine duration; H_0 = extraterrestrial radiation; T_{max}, T_{min} = daily maximum and minimum air temperature.

Ångström–Prescott model

The Ångström–Prescott model relates the clearness index to the relative sunshine duration:

(6)

where H is the measured daily global solar radiation (MJ/m²/day), H_0 is the extraterrestrial radiation (MJ/m²/day), n is the measured daily sunshine duration (h), N is the maximum possible sunshine duration (h), H/H_0 is the clearness index, n/N is the relative sunshine duration, and a and b are dimensionless regression coefficients. The coefficients were determined by ordinary least-squares linear regression of H/H_0 on n/N using all valid days.

Hargreaves–Samani model

The Hargreaves–Samani model estimates the clearness index from the diurnal temperature range:

(7)

where $\Delta T = T_{max} - T_{min}$ is the diurnal temperature range (°C), T_{max} and T_{min} are the daily maximum and minimum air temperatures (°C), and c is an empirical coefficient. The coefficient has no intercept and was obtained by least squares through the origin, $c = \Sigma xy/\Sigma x^2$, where $x = \sqrt{\Delta T}$ and $y = H/H_0$. The coefficient is reported to three decimals, and the unrounded fitted value was used for all estimates.

Model evaluation

Model performance was assessed with the coefficient of determination (R^2), root mean square error (RMSE), mean bias error (MBE) and mean percentage error (MPE), computed between measured (H_m) and estimated (H_e) daily radiation over N_d days:

(8)

(9)

(10)

(11)

where H_m is the measured and H_e the estimated daily global solar radiation (MJ/m²/day), $\bar{H}_m$ is the mean of the measured values, and N_d is the number of days. RMSE and MBE are in MJ/m²/day; MPE is in %. R^2 is dimensionless.

Positive MBE indicates overestimation. Models were evaluated in two ways. First, the full calibration data set was used (calibration performance), which is the basis of the headline coefficients and energy estimates. Second, as an independent check, the data were split 85%/15% (stratified by calendar month, random seed 42) in line with the approach used by Dhakal et al. (2020); the models were refitted on the 1,535 training days and evaluated on the 271 test days. All computations were done in Python using pandas, NumPy and scikit-learn.

Results

Data characteristics and yearly variation

The mean measured daily radiation was 14.34 MJ/m²/day (equivalent to 3.98 kWh/m²/day), the mean sunshine duration was 5.94 h against a mean astronomical day length of 11.99 h, and the mean diurnal temperature range was 11.72 °C. This mean is close to the 14.17 MJ/m²/day reported for the same station by Joshi et al. (2022).

Table 2

Descriptive Statistics of the Daily Data Set (n = 1,806 days)

Variable	Mean	SD	Minimum	Maximum
H (MJ/m²/day)	14.34	5.14	0.33	28.06
n (h)	5.94	3.19	0.00	11.86
N (h)	11.99	1.23	10.24	13.76
H_0 (MJ/m²/day)	32.06	7.13	21.06	40.89
ΔT (°C)	11.72	3.03	2.00	21.80
T_a(°C)	21.97	4.80	9.30	30.60

H = measured daily global solar radiation; n = measured sunshine duration; N = maximum possible sunshine duration; H_0 = extraterrestrial radiation; ΔT = diurnal temperature range; T_a = mean daily air temperature. SD = standard deviation.

Table 3 and Figure 2 show how radiation varies between years. Annual mean H ranged from 13.30 MJ/m²/day in 2021 to 14.96 in 2023, and the mean clearness index from 0.43 to 0.47. Within each year the standard deviation (4.6–5.6) is much larger than the difference between years, so no single year dominates the calibration. The years 2023 and 2025 have fewer valid days (234 and 206) after quality control. The lowest daily radiation of the record, 0.33 MJ/m²/day, was measured on 04 Oct 2025.

Table 3

Yearly Variation of Global Solar Radiation at Dhunibeshi

Year	Valid days	Mean H ± SD (MJ/m²/day)	Maximum H (MJ/m²/day; date)	Minimum H (MJ/m²/day; date)
2020	320	14.32 ± 5.32	27.07 (08 May)	2.17 (16 Nov)
2021	328	13.30 ± 5.36	28.06 (03 Jun)	1.56 (04 Jan)
2022	360	14.93 ± 4.84	26.92 (17 Jun)	0.68 (06 Oct)
2023	234	14.96 ± 5.61	26.67 (05 May)	2.43 (07 Dec)
2024	358	14.66 ± 4.92	25.82 (16 May)	0.91 (27 Sep)
2025	206	13.78 ± 4.57	25.55 (08 Jul)	0.33 (04 Oct)

Note. H values are from valid days only.

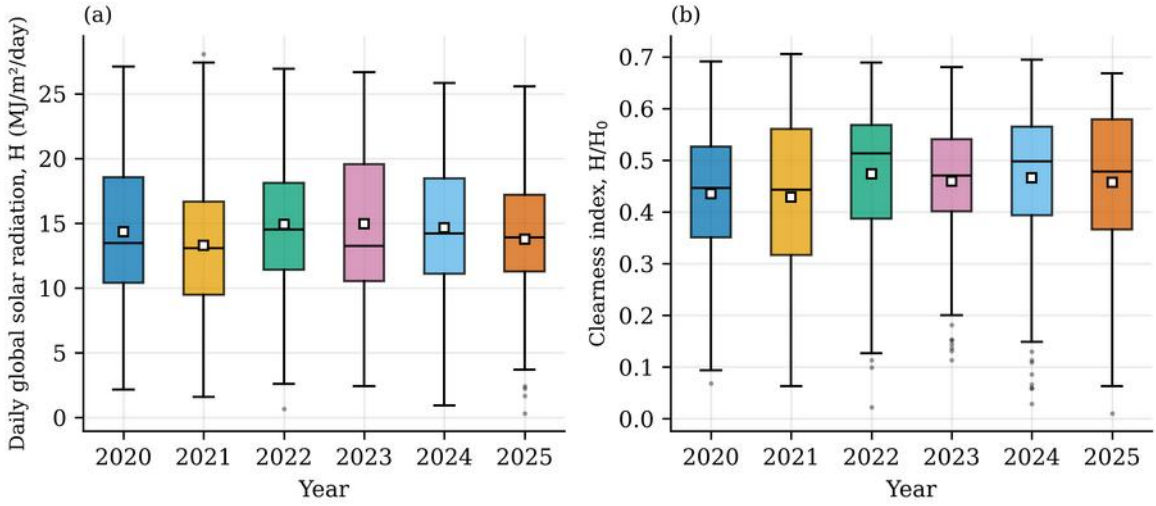


Figure 2

Yearly Variation of Daily Global Solar Radiation and Clearness Index at Dhunibeshi

Boxes show the interquartile range, the line the median, the square the mean and whiskers 1.5 times the interquartile range. (a) Global solar radiation, H; (b) clearness index, H/H_0.

Seasonal and monthly variation

Figure 3 shows the monthly mean of H for each year and averaged over 2020–2025. Averaged over all years, radiation is highest in April (18.68 MJ/m²/day) and lowest in January (10.10). Figure 4 relates this cycle to maximum temperature. Maximum temperature follows H through

the rise to April but peaks later, in June (31.7 °C), and stays high through the monsoon when radiation has already fallen. The drop in H between June and July coincides with the onset of the monsoon, when cloud cover reduces sunshine duration to 2.7 h per day in July.

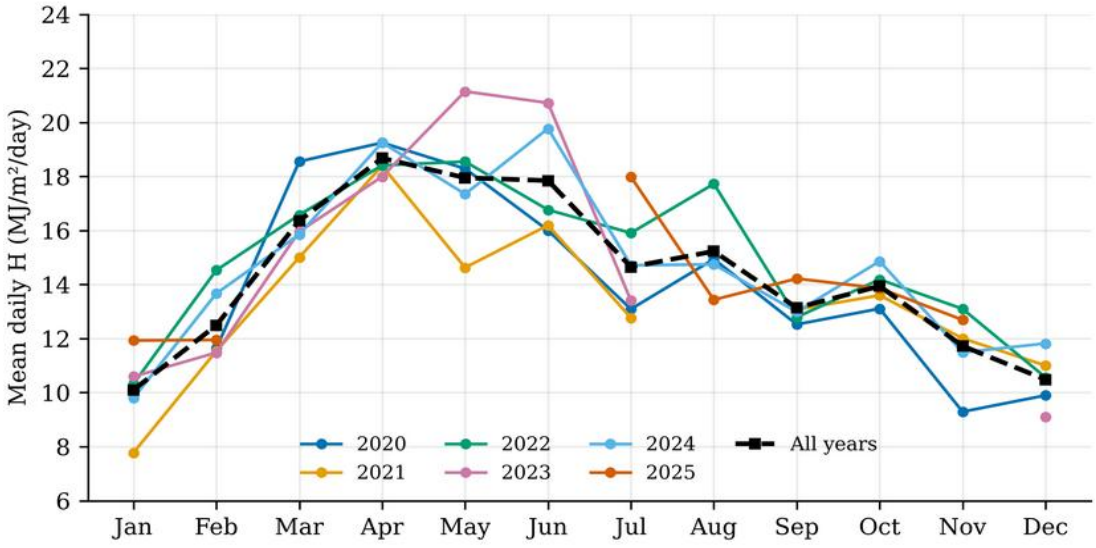


Figure 3

Monthly Mean Daily Global Solar Radiation at Dhunibeshi, 2020–2025

Coloured lines show the monthly mean of each year (months with at least 15 valid days); the dashed black line is the mean of all valid days in each month, 2020–2025.

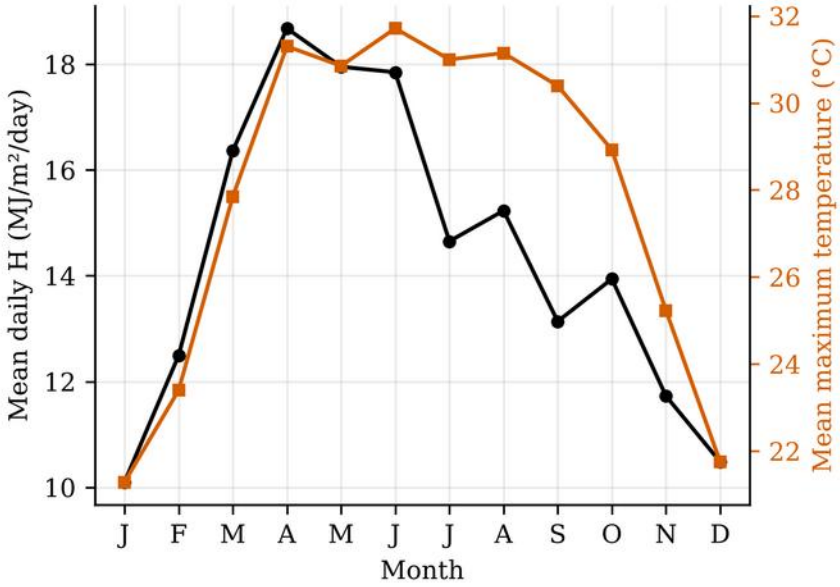


Figure 4

Monthly Mean Daily Global Solar Radiation Compared With Maximum Temperature

Note. Means over 2020–2025 for all valid days. The line with circles is the mean daily H (left axis); the line with squares is the mean daily maximum temperature (right axis).

Figure 5 shows the seasonal means for each year. Pre-monsoon (March–May) is the brightest season in every year, with year means of 16.0–18.7 MJ/m²/day, and winter is the dullest (10.0–11.9). The monsoon shows the largest spread within a season, because clear days and heavy-cloud days alternate. The post-monsoon bar for 2023 is missing because of the sensor fault.

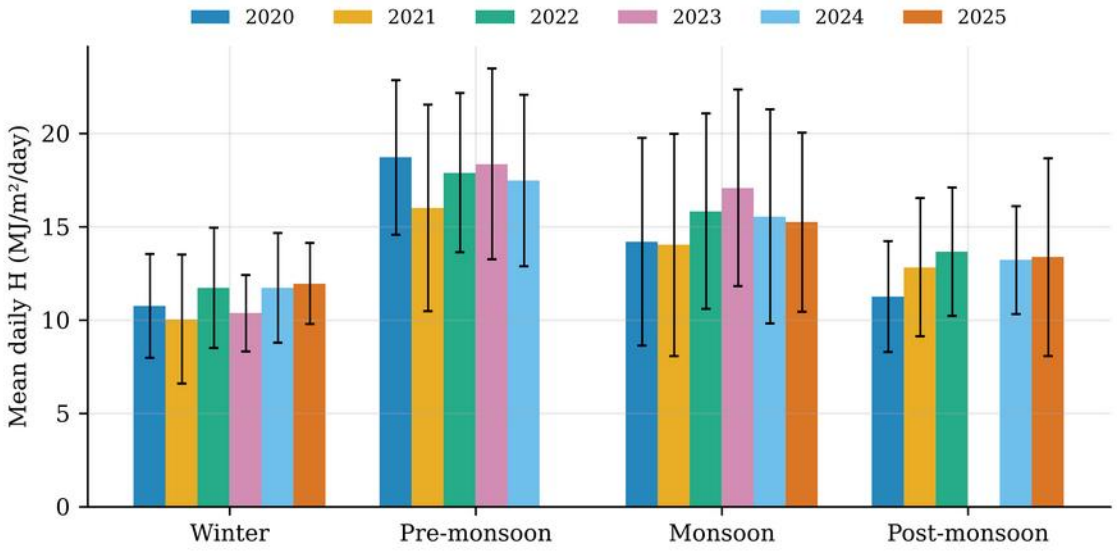


Figure 5

Seasonal Mean Daily Global Solar Radiation at Dhunibeshi for Each Year

Note. Error bars show one standard deviation of the daily values. Winter = Dec–Feb; pre-monsoon = Mar–May; monsoon = Jun–Sep; post-monsoon = Oct–Nov.

Correlation of radiation with sunshine and temperature range

Table 4 gives the Pearson correlation of H and of the clearness index with relative sunshine duration and with ΔT. The clearness index is more strongly correlated than H with both predictors (r = 0.85 against 0.50 for n/N, and 0.67 against 0.39 for ΔT, all days), which is why both models are written in terms of the clearness index, as Joshi et al. (2021) also did. In every year, relative sunshine duration is the stronger predictor of the clearness index, with r between 0.71 and 0.94 against 0.55 to 0.76 for ΔT.

Table 4

Correlation of Global Solar Radiation and Clearness Index With Relative Sunshine Duration and Diurnal Temperature Range

Year	H with n/N	H with ΔT	H/H_0 with n/N	H/H_0 with ΔT
2020	0.438	0.474	0.755	0.730
2021	0.689	0.524	0.936	0.758
2022	0.470	0.367	0.906	0.685
2023	0.426	0.289	0.709	0.552
2024	0.458	0.322	0.867	0.614
2025	0.493	0.346	0.895	0.725
All days	0.504	0.392	0.854	0.675

Note. Values are Pearson correlation coefficients (r) computed on daily data. The last row uses all valid days.

Calibrated coefficients

The Ångström–Prescott regression gave $a = 0.242$ *and* $b = 0.417$, *so* $a + b = 0.66$. Sunshine fraction explained 73% of the variance in the clearness index (Figure 6). The Hargreaves–Samani coefficient was c = 0.135. Fitting each year separately (Table 5) gives a between 0.196 and 0.303, b between 0.296 and 0.492, and c between 0.128 and 0.142, so the multi-year values are a compromise between years.

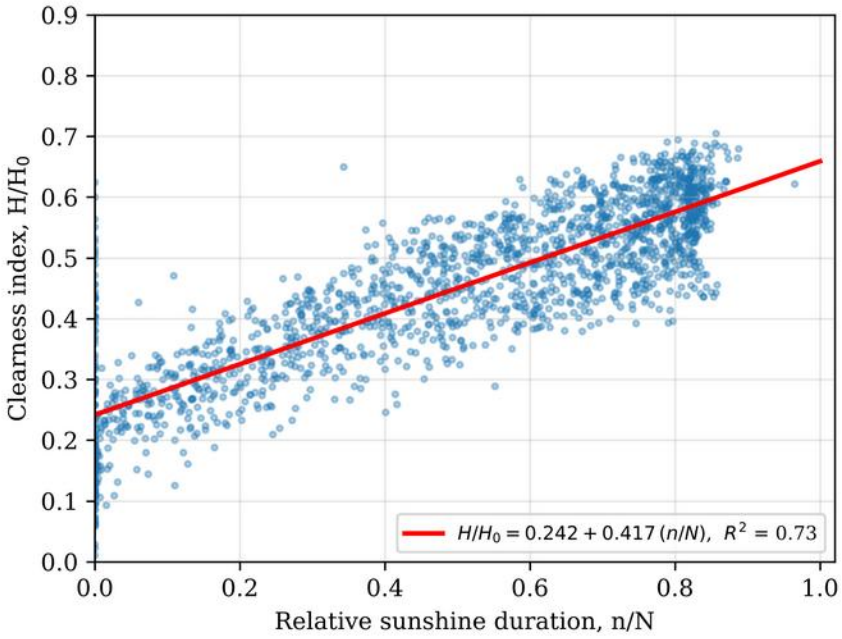


Figure 6

Relationship Between Clearness Index and Relative Sunshine Duration at Dhunibeshi

Note. Each point is one day (n = 1,806). The line is the fitted Ångström–Prescott regression.

Model performance

Table 5 lists the error statistics and fitted constants for each year and for all days, with the better model for each statistic in bold. The Ångström–Prescott model had the higher R^2 and the lower RMSE in 6 of 6 years and the lower MPE in all of them. Its R^2 ranged from 0.68 in 2020 to 0.89 in 2021, while the Hargreaves–Samani R^2 stayed between 0.51 and 0.62. Mean bias was small for both models (|MBE| ≤ 0.31 MJ/m²/day), and neither was consistently less biased: Hargreaves–Samani had the smaller absolute MBE in 3 of 6 years.

Table 5

Statistical Indicators and Empirical Constants of the Models by Year

Year	Model	MPE (%)	MBE (MJ/m²/day)	RMSE (MJ/m²/day)	R^2	*a*	*b*	*c*
2020	Ångström–Prescott	**7.46**	−0.183	**3.027**	**0.675**	0.276	0.356	–
	Hargreaves–Samani	11.32	**0.130**	3.377	0.596	–	–	0.137
2021	Ångström–Prescott	**3.99**	**−0.067**	**1.811**	**0.885**	0.196	0.492	–
	Hargreaves–Samani	16.72	0.311	3.653	0.534	–	–	0.128
2022	Ångström–Prescott	**4.65**	**−0.160**	**1.828**	**0.857**	0.234	0.445	–
	Hargreaves–Samani	12.37	0.227	3.384	0.509	–	–	0.137
2023	Ångström–Prescott	**5.18**	−0.159	**2.681**	**0.771**	0.303	0.296	–
	Hargreaves–Samani	8.32	**−0.080**	3.474	0.615	–	–	0.130
2024	Ångström–Prescott	**6.33**	−0.150	**2.129**	**0.812**	0.221	0.441	–
	Hargreaves–Samani	12.84	**0.132**	3.336	0.539	–	–	0.136
2025	Ångström–Prescott	**14.67**	**−0.184**	**2.042**	**0.799**	0.236	0.448	–
	Hargreaves–Samani	22.75	0.242	3.194	0.509	–	–	0.142
All days	Ångström–Prescott	**7.04**	**−0.142**	**2.346**	**0.792**	0.242	0.417	–
	Hargreaves–Samani	13.69	0.163	3.442	0.552	–	–	0.135

Note. Bold values are the better of the two models for that statistic (higher R^2; lower RMSE, |MBE| and |MPE|).

Table 6 compares calibration and independent test performance with the coefficients used in this paper. On the calibration data, the Ångström–Prescott model gave R^2 = 0.79, RMSE = 2.35 MJ/m²/day and MBE = −0.14 MJ/m²/day; the Hargreaves–Samani model gave R^2 = 0.55, RMSE = 3.44 MJ/m²/day and MBE = 0.16 MJ/m²/day. On the independent 15% test set the ranking was unchanged (Figure 7): R^2 = 0.77 against 0.54, and RMSE = 2.22 against 3.17 MJ/m²/day. The small drop in Ångström–Prescott accuracy between calibration and test data shows that the fit is not overfitted. The coefficients re-estimated on the training subset (a = 0.239, b = 0.422, c = 0.135) are almost identical to the full-sample values.

Table 6

Calibration and Independent Test Performance of the Models for Daily Global Solar Radiation

Data set	Model	R^2	RMSE (MJ/m²/day)	MBE (MJ/m²/day)	MPE (%)
Calibration (n = 1,806)	Ångström–Prescott	0.79	2.35	−0.14	7.04
	Hargreaves–Samani	0.55	3.44	+0.16	13.69
Test (n = 271)	Ångström–Prescott	0.77	2.22	−0.11	5.17
	Hargreaves–Samani	0.54	3.17	+0.22	10.15

Note. Calibration rows use the coefficients fitted on all days. Test rows use coefficients refitted on the 85% training subset. MPE is inflated by overcast days with very low radiation.

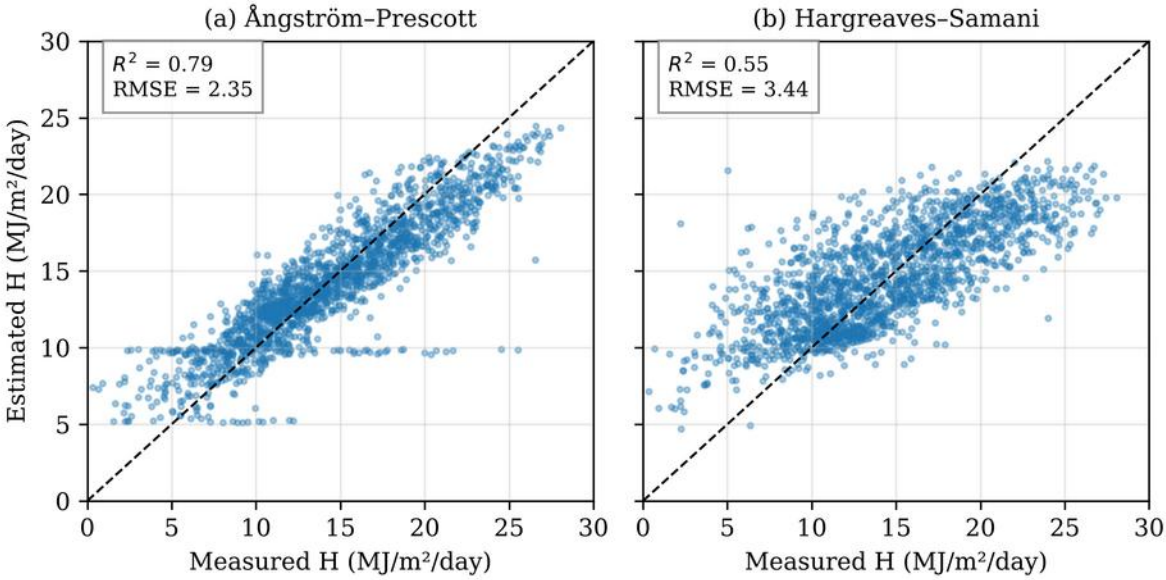


Figure 7

Measured Versus Estimated Daily Global Solar Radiation (Calibration Data)

Note. The dashed line is the 1:1 line. (a) Ångström–Prescott; (b) Hargreaves–Samani.

Aggregating to monthly means improves agreement for both models (Figure 8): R^2 = 0.86 for Ångström–Prescott and 0.82 for Hargreaves–Samani over the 61 months with at least 15 valid days. The gap between the models is therefore much smaller for monthly than for daily estimates, which suggests that the temperature-based model captures the seasonal cycle but not day-to-day cloud variation.

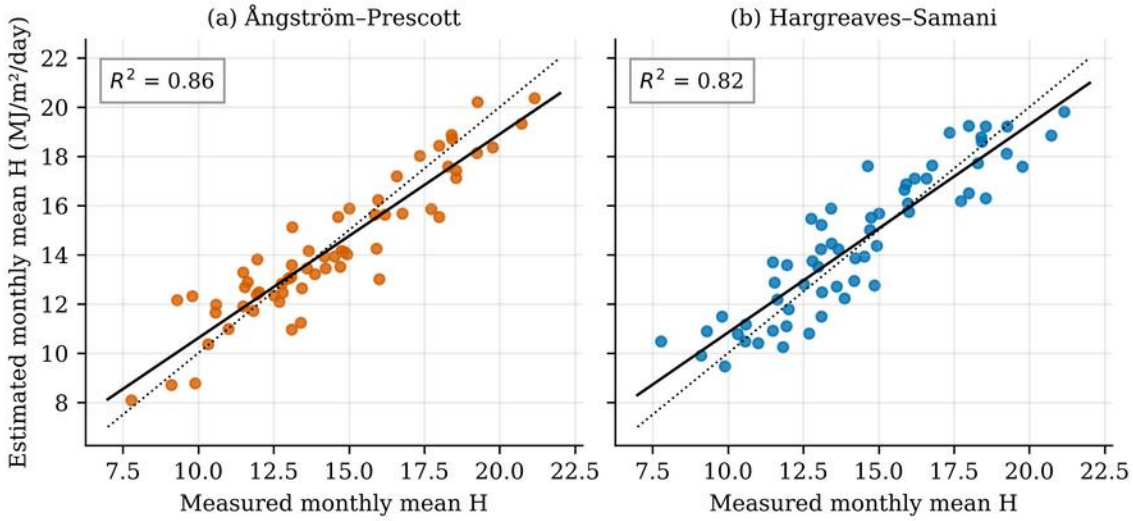


Figure 8

Measured Versus Estimated Monthly Mean Global Solar Radiation

Note. Each point is one month. Solid line: linear fit; dotted line: 1:1 line. (a) Ångström–Prescott; (b) Hargreaves–Samani.

Estimated solar energy

The measured mean daily radiation was 14.34 MJ/m²/day. The Ångström–Prescott model estimated 14.20 MJ/m²/day and the Hargreaves–Samani model estimated 14.51 MJ/m²/day, which are 1.0% below and 1.1% above the measured mean. The measured mean corresponds to about 3.98 kWh/m²/day, or roughly 1,454 kWh/m² per year.

Discussion

The sunshine-based model is clearly more accurate than the temperature-based model at Dhunibeshi (R^2 0.79 versus 0.55; RMSE 2.35 versus 3.44 MJ/m²/day). This is physically reasonable. Sunshine duration records directly how much of the day the sun was unobstructed by cloud, whereas the diurnal temperature range is only an indirect proxy for cloudiness. In a mountain setting, temperature is also shaped by terrain, valley winds and humidity, which weaken the link between temperature range and radiation. Hargreaves and Samani built their model for estimating evapotranspiration (Hargreaves & Samani, 1985), and the coefficient calibrated here (c = 0.135) is lower than the value of 0.16 recommended by FAO-56 for interior sites (Allen et al., 1998). This suggests that generic coefficients would overestimate radiation here, and local calibration is needed. We offer the terrain explanation as a plausible hypothesis, since we did not test it directly.

The Ångström–Prescott coefficients agree well with the published values for the same station. Joshi et al. (2022) reported a = 0.235 and b = 0.432 for Dhunibeshi, with RMSE = 2.363 and MBE = −0.161 MJ/m²/day; we obtained a = 0.242, b = 0.417, RMSE = 2.35 and MBE = −0.14. That an independent, more recent record reproduces the earlier calibration gives confidence in the data and the quality-control procedure. The mean measured radiation (14.34 MJ/m²/day) is also close to their 14.17. The accuracy of the Ångström–Prescott model here is close to the multi-station result of Joshi et al. (2022), and for a model that needs only sunshine duration it is comparable to the best temperature-based model at Biratnagar (R^2 = 0.7498; Dhakal et al., 2020). We note that the two studies use different stations and metrics, so this comparison is indicative only.

Calibrating each year separately shows that the constants are not fixed. The yearly a ranged from 0.196 to 0.303 and b from 0.296 to 0.492, and Joshi et al. (2021) found a similar spread for Kathmandu (a = 0.118–0.348 and b = 0.221–0.566 for the sunshine-only model across four years). A multi-year calibration, as used here, is therefore preferable to a single-year one.

For energy planning, the measured mean of 14.34 MJ/m²/day (3.98 kWh/m²/day) falls within the national range of 3.6–6.2 kWh/m²/day reported by Poudyal (2015), in the lower half of it, so solar energy is viable at this mid-hill site. The reliable, site-calibrated estimates provided here can feed solar resource assessments, photovoltaic sizing and distributed generation planning. Solar and hydropower generation face different hazards, because a flood that damages river-based plants (Shastry, 2026) leaves sunshine unaffected. Solar capacity can therefore reduce the risk of depending on a single resource, which supports the energy-mix argument made in the

Introduction. Sizing the mix would need a full system analysis, which is beyond the scope of this paper.

Limitations

The results come from a single station and about six years of data, so the coefficients should not be transferred to other sites without checking. Four months of sunshine data were lost to a sensor fault and further months to missing data. Temperature data are daily extremes from manual observation. Both models use one set of coefficients for the whole year, so they cannot capture seasonal differences in the relation between sunshine, temperature and radiation. MPE is inflated by low-radiation days and should be read together with RMSE and MBE. Finally, the test set is a random subset of days from the same period, not a different year or site, so it measures interpolation rather than transferability.

Conclusion

This study calibrated and compared the Ångström–Prescott and Hargreaves–Samani models for estimating daily global solar radiation at Dhunibeshi, Dhading, Nepal, using 1,806 quality-controlled days from 2020–2025. The Ångström–Prescott coefficients were *a = 0.242 and b = 0.417, and the Hargreaves–Samani coefficient was c = 0.135.* The sunshine-based model was substantially more accurate (R^2 = 0.79, RMSE = 2.35 MJ/m²/day) than the temperature-based model (R^2 = 0.55, RMSE = 3.44 MJ/m²/day), and its coefficients agree with earlier published values for the same station. The mean available solar energy is about 14.34 MJ/m²/day (3.98 kWh/m²/day). We recommend the Ångström–Prescott model wherever sunshine records exist and the locally calibrated Hargreaves–Samani model only as a fallback. Future work should test season-specific coefficients, add stations across elevation zones, and try machine-learning methods, such as random forests (Breiman, 2001), that use sunshine and temperature predictors together.

Funding

The authors received no financial support for the research, authorship, or publication of this paper.

Conflict of Interest

The authors declare no conflict of interest.

Data Availability

The meteorological data were obtained from the Department of Hydrology and Meteorology, Government of Nepal, and are subject to its data-sharing conditions. The processed daily data set and the analysis code are available from the corresponding author on reasonable request.

References

Akinoğlu, B. G. (1991). A review of sunshine-based models used to estimate monthly average global solar radiation. *Renewable Energy, 1*(3–4), 479–497. https://doi.org/10.1016/0960-1481(91)90061-S

Allen, R. G., Pereira, L. S., Raes, D., & Smith, M. (1998). *Crop evapotranspiration: Guidelines for computing crop water requirements* (FAO Irrigation and Drainage Paper 56). Food and Agriculture Organization of the United Nations.

Ångström, A. (1924). Solar and terrestrial radiation. Report to the international commission for solar research on actinometric investigations of solar and atmospheric radiation. *Quarterly Journal of the Royal Meteorological Society, 50*(210), 121–126. https://doi.org/10.1002/qj.49705021008

Breiman, L. (2001). Random forests. *Machine Learning, 45*(1), 5–32. https://doi.org/10.1023/A:1010933404324

Dhakal, S., Gautam, Y., & Bhattarai, A. (2020). Evaluation of temperature-based empirical models and machine learning techniques to estimate daily global solar radiation at Biratnagar Airport, Nepal. *Advances in Meteorology, 2020*, Article 8895311. https://doi.org/10.1155/2020/8895311

Duffie, J. A., & Beckman, W. A. (2013). *Solar engineering of thermal processes* (4th ed.). John Wiley & Sons. https://doi.org/10.1002/9781118671603

Hargreaves, G. H., & Samani, Z. A. (1985). Reference crop evapotranspiration from temperature. *Applied Engineering in Agriculture, 1*(2), 96–99. https://doi.org/10.13031/2013.26773

Joshi, U., Karki, I. B., Chapagain, N. P., & Poudyal, K. N. (2021). Prediction of daily global solar radiation using different empirical models on the basis of meteorological parameters at Trans Himalaya region, Nepal. *BIBECHANA, 18*(1), 159–169. https://doi.org/10.3126/bibechana.v18i1.29203

Joshi, U., Shrestha, P. M., Maharjan, S., Bhattarai, A., Bhattarai, N., Chapagain, N. P., Karki, I. B., & Poudyal, K. N. (2022). Estimation of solar insolation and Ångström–Prescott coefficients using sunshine hours over Nepal. *Advances in Meteorology, 2022*, Article 3593922. https://doi.org/10.1155/2022/3593922

Poudyal, K. N. (2015). *Estimation of global solar radiation potential in Nepal* [Doctoral dissertation, Tribhuvan University, Institute of Engineering].

Poudyal, K. N. (2016). Estimation of global solar radiation using modified Angstrom empirical formula on the basis of meteorological parameters in Himalaya region Pokhara, Nepal. *Journal of the Institute of Engineering, 11*(1), 158–164. https://doi.org/10.3126/jie.v11i1.14710

Poudyal, K. N., Bhattarai, B. K., Sapkota, B., Kjeldstad, B., & Daponte, P. (2013). Estimation of the daily global solar radiation; Nepal experience. *Measurement, 46*(6), 1807–1817. https://doi.org/10.1016/j.measurement.2013.01.012

Prescott, J. A. (1940). Evaporation from a water surface in relation to solar radiation. *Transactions of the Royal Society of South Australia, 64*, 114–118.

Samani, Z., Hargreaves, G., Tran, V., & Bawazir, S. (2011). Estimating solar radiation from temperature with spatial and temporal calibration. *Journal of Irrigation and Drainage Engineering, 137*(11), 692–696. https://doi.org/10.1061/(ASCE)IR.1943-4774.0000342

Saud, J. S., Shrestha, P. M., Joshi, U., Tiwari, B. R., Karki, I. B., & Poudyal, K. N. (2023). Estimation of global solar radiation using Angstrom and Gopinathan model on sunshine hour and temperature in highland, Nepal. *Molung Educational Frontier, 13*(1), 92–107. https://doi.org/10.3126/mef.v13i01.56094

Shastry, V. (2026, September 3). *Nepal floods test resilience of its hydropower-dependent economy*. Center on Global Energy Policy, Columbia University SIPA. https://www.energypolicy.columbia.edu/nepal-floods-test-resilience-of-its-hydropower-dependent-economy/

Srivastava, R. C., & Pandey, H. (2013). Estimating Angstrom-Prescott coefficients for India and developing a correlation between sunshine hours and global solar radiation for India. *ISRN Renewable Energy*, *2013*, Article 403742. https://doi.org/10.1155/2013/403742

Valiantzas, J. D. (2018). Modification of the Hargreaves–Samani model for estimating solar radiation from temperature and humidity data. *Journal of Irrigation and Drainage Engineering*, *144*(1). https://doi.org/10.1061/(ASCE)IR.1943-4774.0001275

Water and Energy Commission Secretariat. (2010). *Energy sector synopsis report 2010*. Government of Nepal.

Coordinated Frontier Exploration and Victim Localization with a Team of Ground Robots: A Simulation Study

Rajib Mandal

Department of Mechanical and Aerospace Engineering, Pulchowk Campus, Institute of Engineering, Tribhuvan University
Lalitpur, Nepal
mandalrajib0914@gmail.com

Abstract

In a post disaster situation, the rescue team enters the building without knowing the floor plan or victim position. A team of ground robots can be used to get the floor plfan along with victim location. This study evaluates a ROS 2 Jazzy and Gazebo Harmonic system combining per-robot localization, mapping and navigation with centralized coordinator for map merging, frontier allocation and camera-based victim localization. The central coordinator assigns frontiers every 2s using grid path cost function and one of the rules: nearest, greedy or Hungarian assignment. The baseline is formed by running independent robots. A paired campaign of 110 trial (1-3 robots, 4 strategies, 10 paired trial per condition drawn from 6 start/victim combination) in a indoor environment of 6 × 5 m containing a hall and 3 rooms showed that coordinated allocation reduced exploration time by 1.6–1.8× with two robots and 2.0–2.2× with three (greedy: 99 s, 64 s, 47 s), whereas independent explorers became slower as robots were added (88 s, 115 s, 132 s), drove up to 3.7 times the single-robot distance and re-visited 37–44% of their area. All the 6 coordinated vs independent comparison were significant, and three allocation rules were statistically indistinguishable for only 10 trials. An ArUco detector confirmed victim in 100 out of 110 trials within 9.8 cm, and a YOLOv8n with LiDAR confirmed it in all 40 trials about 10-12 s earlier with 2-3 robots but with larger error. Allocating frontiers and merging maps produces the speed up not merely adding robots.

Keywords: Frontier allocation, ROS 2, Hungarian algorithm, victim detection

Introduction

In a post disaster situation, the rescuers must decide which damaged building or place to go where people are likely trapped, usually without plan of what remain inside. Entering the unknown and unstable structures endanger the rescuer and slow, manual searching costs lives. Multiple ground robots can first enter, map the accessible space and report victims' position so rescuers can go in with map and target position (Liu & Nejat, 2013; Murphy, 2014). However, assigning several robots the same exploration task does not ensure faster completion: robots may revisit rooms, compete at doorways and follow already explored routes so a team of coordinated inexpensive robots, each with 2D LiDAR, a small camera and a single-board computer, is therefore attractive.

This study addresses how much coordinator adds, which allocation rule to use and how reliable a camera- equipped team finds a victim. The contributions are an open, end to end ROS 2 simulation system and paired evaluation of team size, exploration efficiency and victim detection. This study addresses a simplified indoor search task motivated by disaster response; it does not evaluate deployment in damaged buildings.

Literature review

Murphy (2014) documents robot deployments after earthquake and building collapses and emphasis the identification of victims and mapping as a main use. Coordinated frontier exploration balance travel cost and information utility across robots (Burgard et al., 2005). Hungarian assignment provides optimal solution for one-to-one assignment (Kuhn, 1955) although assignment in one instant may not minimize an entire mission. The DARPA Subterranean Challenge gave the complete autonomous multi-robot search system to date (Agha et al., 2021; Tranzatto et al., 2022) but rely on 3D LiDAR and custom high-end platforms and do not applicable for low-cost team build with open-sourced standard components. Market-based methods auction targets (Zlot et al., 2002), and segmentation-based methods assign whole rooms (Wurm et al., 2008). Assigning one frontier per robot is an instantaneous single-task, single-robot assignment problem (Gerkey & Matarić, 2004), solvable optimally by the Hungarian method (Kuhn, 1955); greedy assignment is a fast approximation. The strategy rankings depend on environment and implementation details (Faigl and Kulich, 2015). ArUco fiducial markers give reliable, precisely localized detections (Garrido-Jurado et al., 2014) reliable for simulation. YOLO recognizes people without marker, but it gives only direction so actual distance must come from other sensors (Jocher et al., 2023; Redmon et al., 2016).

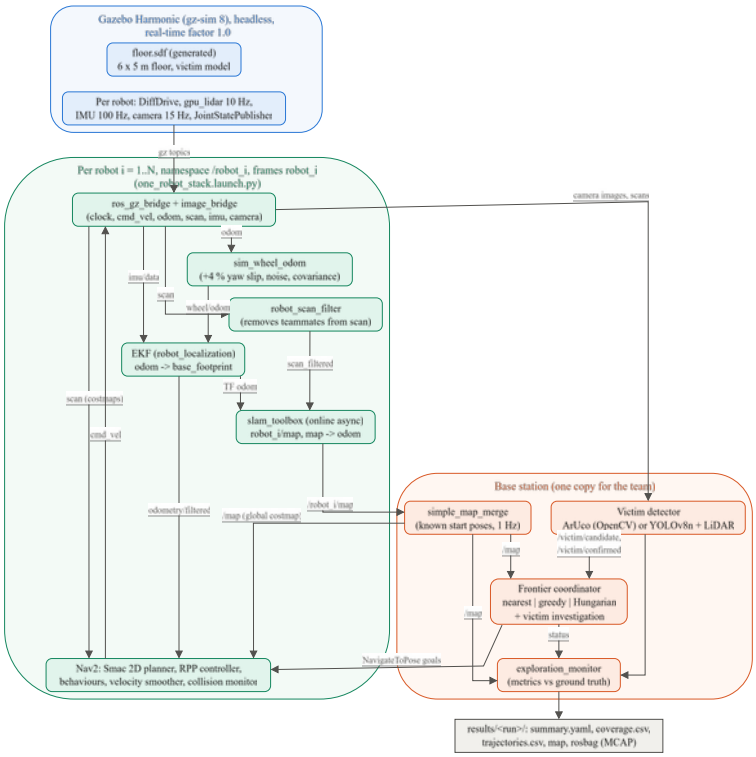
Classic studies establish that coordination helps, but with custom software and few runs per condition and to our knowledge few paired statistical comparisons. No reproducible as well as quantitative study examined a low-cost team built entirely from current ROS 2 components and then compared with common explore_lite (Hörner et al.) baseline and victim detection by each robot.

Materials and Methods

System overview

Each robot run a similar stack with an extended Kalman filter that fuses wheel odometry with IMU data (Moore & Stouch, 2016), slam_toolbox for 2D graph SLAM (Macenski & Jambrecic, 2021), and Nav2 with a Smac 2D planner and the Regulated Pure Pursuit controller (Macenski et al., 2020). A filter removes other robot from a LiDAR scan before SLAM, so that it doesn’t map others as a wall. A centralized base station runs the map merger, frontier coordinator and the victim detector. All the communication happens using standard ROS 2 topics and actions so that same node can be run without change on hardware.

Figure 1

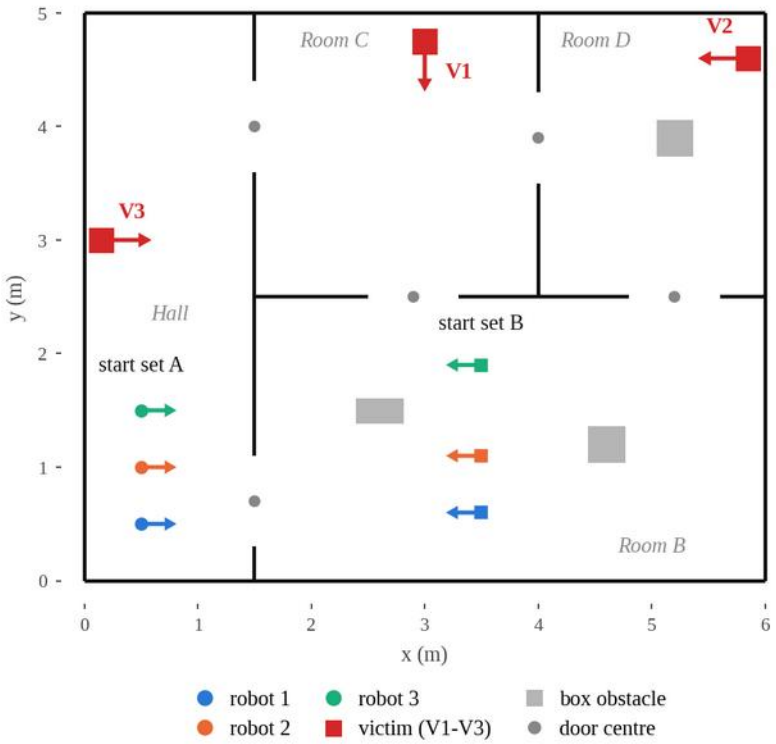


System architecture. Each robot runs sensor fusion, SLAM and navigation; the base station merges maps, allocates frontiers, processes victim observations and evaluates performance against simulation ground truth.

Robot and simulation environment

Each simulated robot was a differential drive with a body of 0.2×0.16 m body, an IMU(100 Hz), forward facing camera (640 × 480, 62° horizontal field of view, 15 Hz), and a 360° 2D LiDAR (10 Hz, 12 m range, σ = 1 cm). The test floor (Figure 2) measures 6 × 5 m and contains a hall, three rooms, five 0.8 m doors, two loops and three box obstacles. The Gazebo world and ground truth occupancy grid(0.05 m cells) are generated from a single floor- plan file so that every map can be scored by cells. Before experimental campaign odometry, sensor fusion, mapping, and navigation were validated against ground truth. EKF reduced the yaw error from +72.1° to −0.02° over 5 spins, SLAM produced a map with 100% wall precision, and Nav2 passed all navigation tests.

Figure 2



The 6 × 5 m Floor with robot sets and Victim position

Map Merging

The base station merged the robot occupancy at 1 Hz. Each local robot transfer data to base station, then it creates common map using robots' position and orientation. The resulting map supported a centralized frontier detection and each robot's global navigation cost map. LiDAR returns whose endpoint lie within 0.27 m of another robot's estimated position is removed by scan filter so that it doesn't register as walls.

Frontier Coordination and allocation Rules

The coordinator updates frontier for each robot every 2 s or when navigation goal is complete. The coordinator identifies frontier cell (free shells with 4 unknow neighbor) and groups them into 8- connected clusters. Cluster shorter than 0.5 m are ignored. The gain, g_f of a cluster is its length, and its goal is the cluster cell nearest the centroid that is at least 0.20 m from any wall. The travel cost C_{rf} from robot r to frontier f is the shortest path length (by Dijkstra) over cells at least 0.15 m from obstacles. The score of sending robot r to frontier f is

(1)

where $\lambda = 0.5$ is the cost weight and $h = 2$ m are a hysteresis bonus given when f is already the robot's target ($\delta_{rf} = 1$, otherwise 0), which prevents oscillation between almost equal frontiers.

Three allocation rules were used

Nearest: Each robot selects its own frontier based on lowest cost reachable frontier. Multiple robots can go to same frontier.

Hungarian: the optimal one-to-one allocation solves the linear assignment problem exactly (Kuhn, 1955)

(2)

subject to

Greedy: Robot-frontier pair is compared, and best remaining is assigned repeatedly and after each assignment to the frontier f^* the gain of every frontier near it is discounted following adapted from of Burgard et al. (2005):

(3)

with R = 1.5 m. Goals are re-sent only if the target moves more than 0.5 m. For robustness two rules were set

i) A frontier still present after 5 s after its goal was reached were blacklisted because the frontier in LiDAR shadows behind the box cannot be cleared.

ii) Exploration was declared complete after two empty cycles or not been reachable for 15s.

Victim Detection and Investigation

The primary campaign represented the victim as box of 0.2m with 0.1 m ArUco marker. Consistent vertical marker faces were selected. A complementary campaign used a YOLOv8n (COCO class person, confidence ≥ 0.5) on a person-shaped doll. The image column corresponding to the detected bounding box determines the bearing, while the LiDAR-based distance d_L is calculated as the median range of points within the central 60% of the bounding box width. Only points located within 0.15 m of the nearest detected point are considered, thereby filtering out background surfaces, such as walls behind the person. A detection is considered valid when the LiDAR-measured distance d_L is consistent with the distance estimated from the bounding box height, h_{px}, assuming a person height of H_p. This condition is expressed as:

(4)

Every validated detection within the specified maximum detection range (2 m for ArUco and 4 m for YOLO) is classified as a hit. Observations were transformed into a common frame, and the victim positions were evaluated using component wise median of accepted detections. Three detections within 2 seconds confirmed the victim.

Experimental Design

Primary campaign (team size, n=1,2 3) comprised with 110 trial across 11 condition with 10 trial of each with strategy (independent, nearest, greedy, Hungarian). One robot Hungarian is identical to greedy giving only 11 conditions.

Every condition ran on the same 10 paired trial configuration, alternating 2 start sets and cycling 3 victim position. These configurations included repeated start-victim position. Running all conditions on the same layout allows each comparison to be made within specific layout and removing layout-to-layout variance. In each of the primary campaigns the team explored the whole floor even after finding the victim position and ended when coordinator or every independent explorer reported completion. Campaigns were limited by 900 s timeouts. A stall

was registered when coverage increased only 0.2% over 120 s and total robot motion below 0.2m over 60s. Stalled trials were excluded from time statistics. A complementary campaign of 40 trials repeated over four conditions (1-3 robots greedy. 2 robots independent)

Metrics and Statistical Analysis

All the metrics were computed against Gazebo ground truth. Performance was evaluated using exploration time, total travel distance, map coverage, exploration overlap, wall F1 score, robot localization error, victim confirmation rate, confirmation time, and positional error. Exploration time doesn't account for returning home travel. Overlap was the share of visited 0.25 × 0.25 m cells visited by two or more robots. Coverage measures the proportion of ground-truth free cells mapped as free. Wall precision and recall used a 0.1 m matching tolerance.

Paired speed-up was calculated by dividing the single-robot exploration time by the team exploration time for the same strategy and trial configuration. The paired speed-up for layout *j* is

(5)

Hungarian allocation used the corresponding single-robot greedy trial as its reference. Only pairs in which both trials completed contributed to speed-up estimates and time comparisons. Hypotheses were tested with two-sided exact Wilcoxon signed-rank tests on the ten paired layouts (Wilcoxon, 1945); the smallest attainable p is .002. The Holm (1979) correction was applied within pre-defined families: coordination (independent vs. each coordinated rule at $n = 2$, 3; six tests), rule (pairs of coordinated rules; six tests) and team size (four tests). Descriptive results are reported as mean ± 95% confidence-interval half-width

Results

Exploration was completed in 109 out of 110 ArUco trials (Primary campaign) and 39 out of 40 in YOLO trials (complementary campaign).

Exploration Time and Scaling with Team Size

Table 1 and Figure 3 show the central result of primary campaign. With coordination exploration became faster with each robot added while independent exploration became slower. Coordinated robots achieved paired speed up of 1.61-1.79 times with 2 robots and 1.96- 2.18 times with 3 robots. Greedy and Hungarian beats the single robot on all ten layouts with 3 robots. The coordination even reduced the spread of time thus making it more predictable. The independent baseline took 87.8 s, 115.1 s and 132.2 s (speed-ups 0.79× and 0.67×), and 2 or 3 independent robots were slower than 1 on every layout.

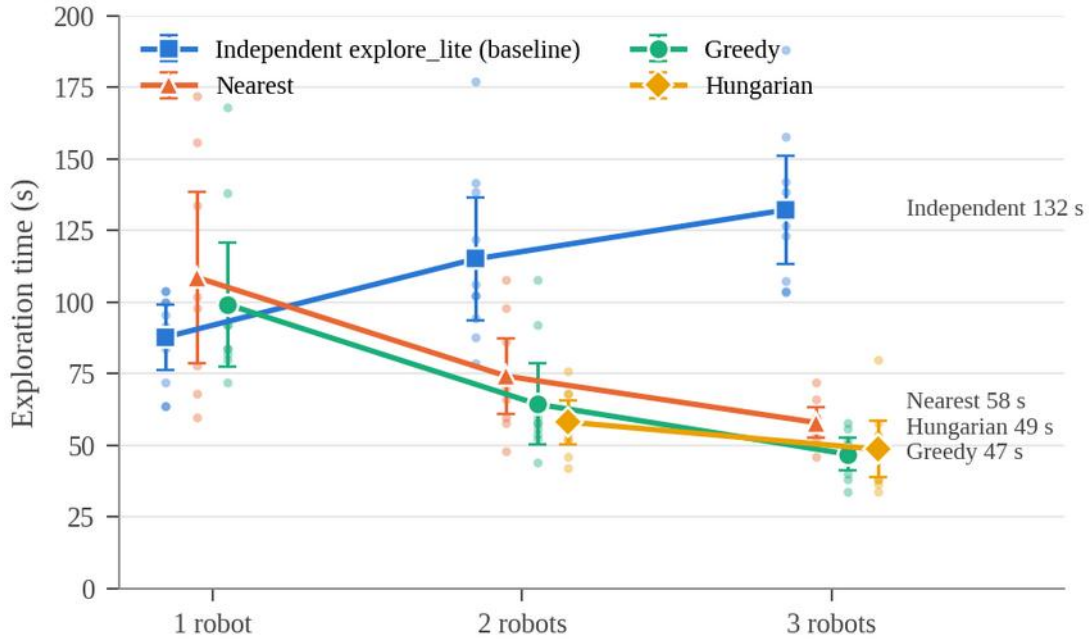
Table 1

Exploration Results per conditions

n	Strategy	Completed	Time (s)	Speed-up	Distance (m)	Overlap (%)
1	Independent	10/10	87.8 ± 11.4	–	12.8 ± 1.6	–
1	Nearest	9/10	108.7 ± 29.8	–	12.8 ± 2.3	–
1	Greedy	10/10	99.2 ± 21.6	–	12.8 ± 1.2	–
2	Independent	10/10	115.1 ± 21.4	0.79 ± 0.11	29.6 ± 5.2	37.0
2	Nearest	10/10	74.2 ± 13.2	1.61 ± 0.65	17.0 ± 1.2	5.9
2	Greedy	10/10	64.4 ± 14.1	1.67 ± 0.52	18.0 ± 2.3	11.2
2	Hungarian	10/10	58.2 ± 7.7	1.79 ± 0.56	17.2 ± 1.7	6.5

n	Strategy	Completed	Time (s)	Speed-up	Distance (m)	Overlap (%)
3	Independent	10/10	132.2 ± 18.9	0.67 ± 0.06	47.1 ± 4.8	44.3
3	Nearest	10/10	58.0 ± 5.2	1.96 ± 0.61	22.8 ± 2.3	6.8
3	Greedy	10/10	47.0 ± 5.6	2.18 ± 0.56	19.9 ± 1.5	10.1
3	Hungarian	10/10	48.6 ± 9.9	2.17 ± 0.56	20.4 ± 2.6	8.6

Figure 3



Exploration Time Against Team Size

Note. Mean ± 95% CI over completed trials; faint dots are single trials on the same ten layouts.

Statistical Test

Table 2 presents the results of the paired statistical tests. All six comparisons between coordinated and independent approaches showed statistically significant differences (adjusted p = .012, the minimum achievable value after correction). For the greedy allocation method, execution time decreased significantly when the number of robots increased from one to two and from two to three. In contrast, the independent baseline showed a significant increase in execution time when moving from one to two robots. No statistically significant differences were observed among the allocation strategies after correction. The nearest and Hungarian methods with two robots showed the closest result to significance (uncorrected p = .010; adjusted p = .059). For the single-robot configuration, no statistically significant difference was found between the coordinator and explore_lite (p = .56).

Table 2

Paired Wilcoxon Signed-Rank Test on Exploration Time

Family	Comparison (robots)	Median Δ (s)	Wins	p	p_H
Coordination	Independent vs. Nearest (2)	+31.1	8/10	.010	.012*
	Independent vs. Greedy (2)	+41.4	10/10	.002	.012*
	Independent vs. Hungarian (2)	+54.1	10/10	.002	.012*
	Independent vs. Nearest (3)	+71.6	10/10	.002	.012*

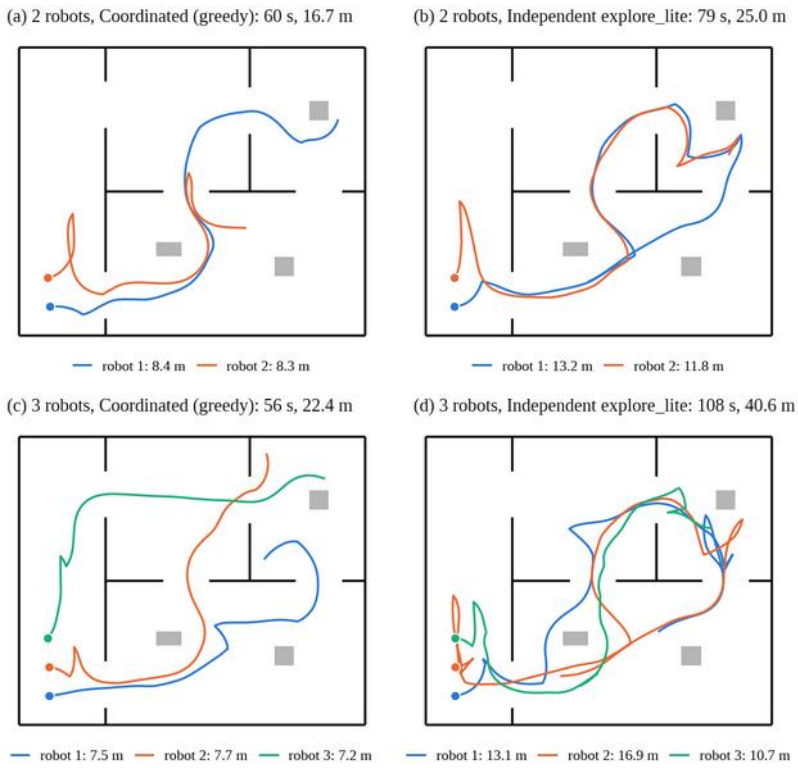
Family	Comparison (robots)	Median Δ (s)	Wins	p	p_H
	Independent vs. Greedy (3)	+79.7	10/10	.002	.012*
	Independent vs. Hungarian (3)	+81.7	10/10	.002	.012*
Rule	Nearest vs. Greedy (2)	+5.9	8/10	.160	.480
	Nearest vs. Hungarian (2)	+12.0	9/10	.010	.059
	Greedy vs. Hungarian (2)	+4.1	6/10	.192	.480
	Nearest vs. Greedy (3)	+8.0	7/10	.049	.244
	Nearest vs. Hungarian (3)	+12.0	7/10	.109	.438
	Greedy vs. Hungarian (3)	−1.0	3/10	.674	.674
Team size	Greedy 1 vs. 2	+30.0	8/10	.014	.027*
	Greedy 2 vs. 3	+9.1	9/10	.006	.018*
	Independent 1 vs. 2	−17.1	0/10	.002	.008*
	Independent 2 vs. 3	−22.3	3/10	.193	.193
Single robot	Independent vs. Greedy (1)	+1.8	5/10	.557	.557

Note. Δ = first minus second condition (positive: second faster). Wins = layouts on which the second condition was faster. p_H = Holm-adjusted within each family. $^*p_H < .05$.

Why Independent robots slow each other down

Two and three independent robots covered 2.3 and 3.7 times the distance than that of one robot (12.8 m) whereas the coordinated robot teams took 1.3-1.8 times more distance. The map overlap was 37% and 44% for the independent robots against 6-11% for any coordination system. The scan filter removes another robot from its SLAM but not from Nav2. Other robots are treated as obstacles, must avoid collision. Each robot starts from 0.5 m apart so two robots may pick same frontier and hence slow down. The door is only 0.8 m and each robot tries to pass by the center of gate, so it passes one after another.

Figure 4



Ground Truth Robot on layout start set A, Victim V1

Note. Coordinated greedy (a, c) versus independent explore_lite (b, d) with two and three robots. Dots mark start poses.

Map Quality and Localization

Median wall F1 ranged from 99.1 -99.9% across all conditions and covered 92-95% free space. The median worst case localization error was 8 cm for all the trials. Five trials suffered false SLAM loop closure between similar looking places, 4 out of 5 occurred among 30 independent trials. independent robots drive longer, repetitive routes with 37–44% overlap. That gives SLAM many more loop-closure attempts, and more chances to accept a wrong one. Deployment would require map consistency checks and recovery policy.

Victim Localization

ArUco confirmed the Victim in 100 of 110 trials, with mean error of 9.8 cm. 8 out of 10 misses have a common configuration, victim V3 in the hall's west well and the robot starting from hall facing east. The LiDAR maps the hall (walls) and no robots turn back its camera toward the west because no frontier gets allocated. So, a floor can be completely mapped while parts of it are never seen by cameras. YOLO and LiDAR configuration confirmed victims in all its 40 trials. Table 3 and figure 5 compare the two detectors in the same layout. YOLO confirmation was 10.6- 11.8 s earlier on average at larger error in position (with mean 5.3-9.3 cm and max of 17.6 cm). Exploration times were unaffected by detector.

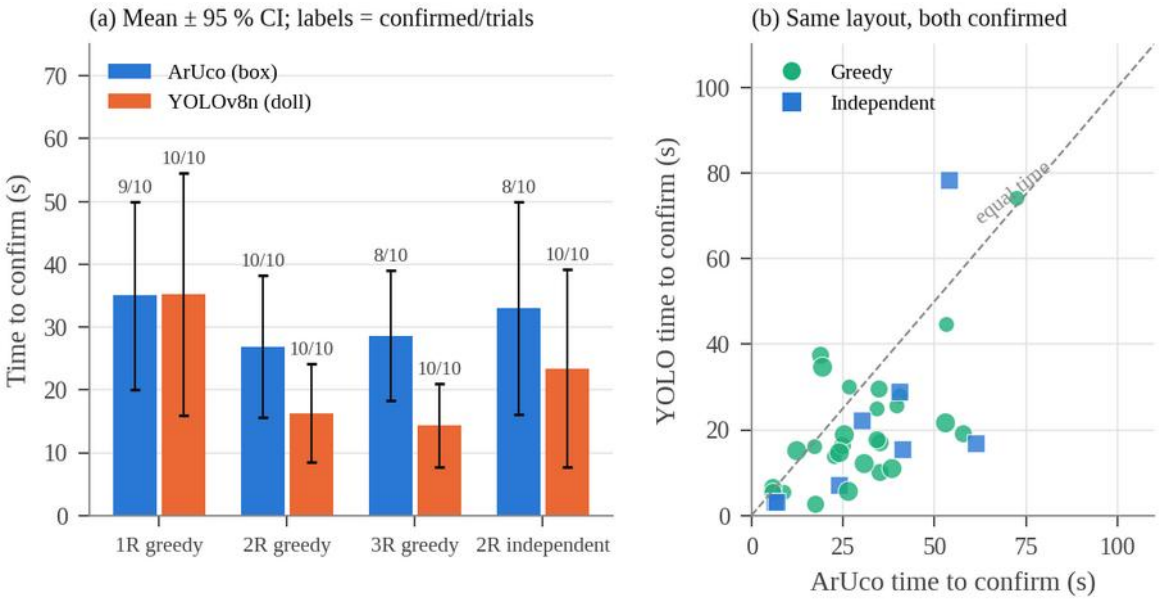
Table 3

Victim Localization with ArUco and YOLOv8n on same layouts for only 40 trials.

n	Strategy	Found ArUco	Found YOLO	Time ArUco (s)	Time YOLO (s)	Error ArUco (cm)	Error YOLO (cm)
1	Greedy	9/10	10/10	35.0	35.3	5.6 / 8.0	6.7 / 9.2
2	Greedy	10/10	10/10	26.9	16.3	4.8 / 8.6	7.5 / 15.3
3	Greedy	8/10	10/10	28.6	14.3	3.5 / 6.0	9.3 / 17.6
2	Independent	8/10	10/10	33.0	23.4	5.1 / 9.8	5.3 / 9.2

Note. Time= mean time for victim confirmation. Error = mean/maximum distance between the confirmed estimate and true victim center. These are 40 paired layouts from complementary campaigns.

Figure 5



Time to confirm the victim with each detector

Note. (a) Mean ± 95% CI over confirmed trials; labels give confirmed/total trials. (b) Paired layouts on which both detectors confirmed the victim; points below the diagonal were faster with YOLO.

Discussion

The result agrees with the principle for coordination exploration described by Burgard et al. (2005) that sharing information reduces the redundancy of exploration. Even nearest allocation benefitted from the merged map because frontiers cleared by one robot disappeared for other. Either of the allocation methods didn't show any statistically established advantage over other in small arena because in small floor with few simultaneous frontiers, Greedy discounting and Hungarian optimality rarely differs. The non-significant rule difference doesn't necessarily mean equality: with ten pairs difference of 10 s cannot be resolved. Uncoordinated robots even block each other, so the time increases on increasing the number of robots. The allocation rules matter far less(and depends on environment) than having one as observed by Faigl & Kulich

(2015) that strategy ranking depends on the environment. Efficiency relative to linear scaling dropped from 80–90% with two robots to 65–73% with three, because a 6 × 5 m floor offers only a few large frontiers at a time and all robots must first cross the same starting area; the useful team size should grow with the number of rooms and doors.

Frontier exploration driven by LiDAR sees 12 m in all direction meanwhile camera only sees 62°, 2–4 m ahead. This setup particularly misses the victim in opposite of initial viewing direction. Camera coverage frontiers or view panning term in score of Equation 1, short spin on entering each room or a longer-range detector (as YOLO demonstrated) would close this gap.

Limitations

The evaluation used just one 6 × 5 m floor with up to 3 robots, so the actual time and exact no of robot will differ from building floor to floor and hardware configurations of robot. The communication was perfect and map merging had a known start position which are harder to achieve in real life. Results cannot establish performance in rubble, smoke, occlusion or unreliable networks.

Physical-robot validation, larger environments and controlled detector comparisons remain necessary. Doesn’t talk about the actual implementation of physical robots.

Conclusion

The paper showed a low-cost ROS2 multi robot system for indoor post disaster evaluated in paired campaign of 150 trials. Coordination and map merging produced a speedup. Frontier allocation made two robots 1.6-1.8 times three -robots 2.0-2.2 times faster than one robot. Independent group of robots slow down on adding robot. The three allocation rules were statistically indistinguishable, maps stayed accurate, and the victim was localized within 10 cm by ArUco in 91% of trials and within 18 cm by a YOLOv8n-plus-LiDAR detector in all trials. Future work should prioritize camera-aware exploration, robust localization and paired hardware experiments with realistic sensing and communication.

Funding

The author received no financial support for the research, authorship, or publication of this paper.

Conflict of Interest

The author declare no conflict of interest.

Author Contributions

The sole author contributed to all aspects of the research, including study design, methodology, experimentation, data analysis, and manuscript preparation.

Data Availability

The simulation software, configuration files, per-trial results and analysis scripts will be available on authors GitHub.

References

Agha, A., Otsu, K., Morrell, B., Fan, D. D., Thakker, R., Santamaria-Navarro, A., Kim, S.-K., Bouman, A., Lei, X., Edlund, J., Ginting, M. F., Ebadi, K., Anderson, M., Pailevanian, T., Terry, E., Wolf, M., Tagliabue, A., Vaquero, T. S., Palieri, M., . . . Burdick, J. (2021). *NeBula: Quest for robotic autonomy in challenging environments; TEAM CoSTAR at the DARPA Subterranean Challenge* (arXiv:2103.11470). arXiv. https://doi.org/10.48550/arXiv.2103.11470

Burgard, W., Moors, M., Stachniss, C., & Schneider, F. E. (2005). Coordinated multi-robot exploration. *IEEE Transactions on Robotics, 21*(3), 376–386. https://doi.org/10.1109/TRO.2004.839232

Faigl, J., & Kulich, M. (2015). On benchmarking of frontier-based multi-robot exploration strategies. In *Proceedings of the European Conference on Mobile Robots (ECMR)*. IEEE.

Garrido-Jurado, S., Muñoz-Salinas, R., Madrid-Cuevas, F. J., & Marín-Jiménez, M. J. (2014). Automatic generation and detection of highly reliable fiducial markers under occlusion. *Pattern Recognition, 47*(6), 2280–2292. https://doi.org/10.1016/j.patcog.2014.01.005

Gerkey, B. P., & Matarić, M. J. (2004). A formal analysis and taxonomy of task allocation in multi-robot systems. *The International Journal of Robotics Research, 23*(9), 939–954. https://doi.org/10.1177/0278364904045564

Holm, S. (1979). A simple sequentially rejective multiple test procedure. *Scandinavian Journal of Statistics, 6*(2), 65–70.

Hörner, J., & robo-friends contributors. (n.d.). *m-explore-ros2: ROS 2 port of explore_lite and multirobot_map_merge* [Computer software]. GitHub. https://github.com/robo-friends/m-explore-ros2

Jocher, G., Chaurasia, A., & Qiu, J. (2023). *Ultralytics YOLOv8* [Computer software]. GitHub. https://github.com/ultralytics/ultralytics

Kuhn, H. W. (1955). The Hungarian method for the assignment problem. *Naval Research Logistics Quarterly, 2*(1–2), 83–97. https://doi.org/10.1002/nav.3800020109

Liu, Y., & Nejat, G. (2013). Robotic urban search and rescue: A survey from the control perspective. *Journal of Intelligent & Robotic Systems, 72*(2), 147–165. https://doi.org/10.1007/s10846-013-9822-x

Macenski, S., & Jambrecic, I. (2021). SLAM Toolbox: SLAM for the dynamic world. *Journal of Open Source Software, 6*(61), Article 2783. https://doi.org/10.21105/joss.02783

Macenski, S., Martín, F., White, R., & Ginés Clavero, J. (2020). The Marathon 2: A navigation system. In *Proceedings of the IEEE/RSJ International Conference on Intelligent Robots and Systems (IROS)* (pp. 2718–2725). IEEE.

Moore, T., & Stouch, D. (2016). A generalized extended Kalman filter implementation for the Robot Operating System. In E. Menegatti, N. Michael, K. Berns, & H. Yamaguchi (Eds.), *Intelligent autonomous systems 13* (pp. 335–348). Springer.

Murphy, R. R. (2014). *Disaster robotics*. MIT Press.

Redmon, J., Divvala, S., Girshick, R., & Farhadi, A. (2016). You only look once: Unified, real-time object detection. In *Proceedings of the IEEE Conference on Computer Vision and Pattern Recognition (CVPR)* (pp. 779–788). IEEE. https://doi.org/10.1109/CVPR.2016.91

Tranzatto, M., Mascarich, F., Bernreiter, L., Godinho, C., Camurri, M., Khattak, S., Dang, T., Reijgwart, V., Löje, J., Wisth, D., Zimmermann, S., Nguyen, H., Fehr, M., Solanka, L., Buchanan, R., Bjelonic, M., Khedekar, N., Valceschini, M., Jenelten, F., . . . Alexis, K. (2022). CERBERUS: Autonomous legged and aerial robotic exploration in the tunnel and urban circuits of the DARPA Subterranean Challenge. *Field Robotics, 2*, 274–324. https://doi.org/10.55417/fr.2022011

Wilcoxon, F. (1945). Individual comparisons by ranking methods. *Biometrics Bulletin, 1*(6), 80–83. https://doi.org/10.2307/3001968

Wurm, K. M., Stachniss, C., & Burgard, W. (2008). Coordinated multi-robot exploration using a segmentation of the environment. In *Proceedings of the IEEE/RSJ International Conference on Intelligent Robots and Systems (IROS)* (pp. 1160–1165). IEEE.

Zlot, R., Stentz, A., Dias, M. B., & Thayer, S. (2002). Multi-robot exploration controlled by a market economy. In *Proceedings of the IEEE International Conference on Robotics and Automation (ICRA)* (pp. 3016–3023). IEEE.